UTRECHT UNIVERSITY

MASTER THESIS

A study on the synthesis of a model CoMnO catalyst for FTO reactions

Author:
Guusje Delen, BSc.

Supervisor:
Jingxiu Xie, MSc.
prof. dr. ir. K.P. De Jong

Universiteit Utrecht

May 2, 2016

Abstract

In this work, the synthesis of a model CoMnO catalyst is described. MnO was used in large amounts (up to 80 wt%) to enhance the lower olefin selectivity of cobalt.

The lower olefin selectivity promotion by MnO was probed by the use of a bulk CoMnO compound. This bulk system was characterised using SEM, XRD and TPR and was used to determine FTO reaction optima (temperature, pressure). TPR indicated that MnO may have a positive effect on the reducibility of cobalt oxide. In a range of 5-20 bar and 220-280 °C, optima were found at 10 bar and 240 °C.

Subsequently, using colloidal synthesis, model CoMnO catalysts were made. Three classes of colloidal particles were synthesised: tripod, tetrahedral and hexagonal colloids of 60, 20 and 16 nm, respectively. These particles were characterised using TEM, STEM-EDX, XRD and XPS. The colloidal particles were made up of a uniform distribution (STEM-EDX) of cobalt and manganese which are present as separate CoO and MnO species (XRD, XPS), in contrast to a mixed CoMnO spinel structure for the bulk system (XRD).

At low pressures (1 bar), the tetrahedral catalyst behaves as a FTS catalyst with C_{5+} as its main fraction (45%) and a lower olefin fraction of 35%. Through the calcination of the tetrahedral particles, the crystal structure was changed to a mixed spinel phase. This crystal structure change resulted in an increased activity, a decreased lower olefin selectivity (24%) and an increased C_{5+} selectivity (60%). It appeared that the crystal structure of the CoMnO was of large influence on the catalytic properties of the catalysts.

Acknowledgements

"The roots of education are bitter, but the fruit is sweet."
– Aristotle

The process of writing this thesis has been challenging and it would have been impossible without the help of some people. First of all, thank you JX, for always starting with something positive before laughing at my latest work. But more, thank you for your guidance, you have made this experience very educational. Your support and critical view have been instrumental throughout this master thesis project.

My gratitude is expressed towards professor Krijn de Jong. Through discussion you have given my work the direction it needed. You have helped me to set realistic goals for myself and thus prevent me getting lost in possibilities.

In the group I'd like some people in particular. I would like to thank Pasi Palaanen for XRD and XANES measurements and for thorough analysis and explanation of the acquired data. Wouter Lamme is thanked for his TEM and STEM-EDX measurements, also Nynke Krans is thanked for TEM measurements. Tom van Deelen and Martin Oschatz are thanked for their input and many fruitful discussions. Marianna Casavola is thanked for providing a framework for the colloidal synthesis from which the research could be started. Marjan Versluijs-Helder is thanked for her help in optimising XRD measurements. Hans Meeldijk is thanked for help during TEM and SEM measurements.

Additionally, I would like to thank Tiny Verhoeven from TU/e for performing XPS measurements.

Many thanks to Lars van der Wal and Bart Sirks, for keeping me company during the sometimes seemingly endless days of work and for support without judgement, as well as the creation of pancake day. Dielis Delen is thanked for his help in creating figures in a much better way than I ever could. Eduard van Ravensberg I'd like to thank for being there at the end of the day and for keeping me sane by driving me insane.

Contents

1

Introduction

Lower olefins C$_2$-C$_4$, or lower, olefins are a group of alkenes that are predominately produced by the steam-cracking of naphtha, a distillation fraction of oil, and have various downstream purposes.[1] In industry, lower olefins are largely used for the polymerisation to plastics and as precursors for chemicals. Over the years the demand for these oil derivatives has increased hugely and the demand will continue to grow.[1] However, the supply of oil varies due to, for example, political instability of oil producing regions. In order to adapt to the change in supply and demand of oil and its derivatives, companies need to innovate.[2]

Additionally, the use of oil has a negative effect on the environment, which adds to the need to find alternative feed stocks. For example, the extraction of oil is accompanied by the production of methane. Economic considerations lead to the flaming, rather than the utilisation, of this methane.[3] This significantly increases the carbon footprint of the oil recovery process. Societal pressure has led to the sharpening of legislation considering the environmental impact of processes and products, for example by setting limits to the contents of fuels in terms of polluting contaminants (NOx, sulphur etc.), contaminants typically found in oil distillation fractions.[4]

Various alternative olefin synthesis routes are known. These routes can be divided into direct and indirect routes. Direct routes are typically preferred, as they require less production steps. An example of an indirect route is the methanol to olefin process. In methanol to olefins synthesis (MTO), methanol is converted to olefins on the acidic sites of zeolites. [5, 6] The methanol used in this MTO process is synthesised prior to methanol conversion, from coal or natural gas. A route closely related to MTO, is dimethyl ether to olefins synthesis (DMTO). It is similar to MTO in the sense that the precursor is synthesised from coal or natural gas, prior to conversion to olefins, i.e. DMTO is another indirect route of olefin synthesis. [7]

Fischer-Tropsch synthesis A suitable direct alternative for the production of lower olefins without the use of oil makes use of Fischer-Tropsch (FT) process, invented by Frans Fischer and Hans Tropsch in war time-Germany, in order to compete with rival countries that had access to oil, which Germany at the time had not.[8] They developed a method to convert a mixture of carbon monoxide and hydrogen gas (synthesis gas, syngas in short) into long olefinic and paraffinic hydrocarbon chains. The general reactions taking place in FT are given in the following equations for paraffins (1.1) and olefins (1.2).[8, 9, 4]

$$nCO + (2n+1)H_2 \longrightarrow C_nH_{2n+2} + nH_2O \tag{1.1}$$

$$nCO + 2nH_2 \longrightarrow C_nH_{2n} + nH_2O \tag{1.2}$$

An additional reaction taking place in FT reactions, is the water-gas shift reaction which is given in equation 1.3. [10, 11, 12].

$$CO + H_2O \leftrightarrow CO_2 + H_2 \tag{1.3}$$

Apart from the advantage of using FT because it circumvents the use of oil, another advantage of Fischer-Tropsch synthesis (FTS) is that it produces very clean fuels, i.e. there is no need for post synthesis purifications such as desulphurisation, a purification which (amongst others) is currently necessary for all oil derived automobile fuels.[3]

Fischer-Tropsch reaction feedstock is produced from either natural gas, coal or biomass, which is converted into syngas, typically done by steam reforming.[3] Dependent on the source used for syngas production, its composition varies: coal and biomass yield H_2 poor syngas, whereas natural gas gives H_2 rich syngas. This syngas can then be catalytically converted into (long) carbon chains. Potential catalysts can be found in group VIII in the periodic table, e.g. Fe and Co.[13]

Influencing the Fischer-Tropsch synthesis selectivity   Initially the FT process was developed to synthesize fuels/gasoline, thus chains of an average length of 5-12 C atoms. These could either be synthesized directly, or through the cracking of even longer carbonaceous chains: wax (C_{18+}). The same principle holds for the production of lower olefins, thus lower olefins can be made by the cracking of long hydrocarbon chains, or one can aim to produce these lower olefins directly.

The challenge lies in the selective production of lower olefins, without by-products of shorter (methane) or longer (C_{5+}) chains. The length of the produced hydrocarbon chains is dependent on various factors, such as catalyst material, temperature, pressure, promoters etc. However, a single set of conditions will not yield a set of single length FT products: a distribution of products is synthesised as is described statistically in the Anderson-Schulz-Flory (ASF) distribution.[14] This model depicts the product distribution of varying product chain lengths dependent on their chain growth probability, α, as shown in Figure 1.1.[1]

$$w_i = i(1-\alpha)^2\alpha^{i\text{-}1} \tag{1.4}$$

Alpha is calculated using the ASF equation (Equation 1.4), where i is the number of carbon atoms, w_i is the weight fraction of chain length i, α is the chain growth probability and $(1-\alpha)$ is the chain termination probability.[3]

One can see that to optimize the yield of lower olefins, an alpha value of ~0.5 is desired. A catalyst known to be able to reach such an alpha value at elevated temperatures is iron. Iron is indeed used for the direct production of lower olefins through FT reactions (FTO) [1, 15]. Iron is an abundant, cheap catalyst, however it is not ideal: iron tends to deactivate due to carbonaceous deposits on the catalyst surface. This is due to
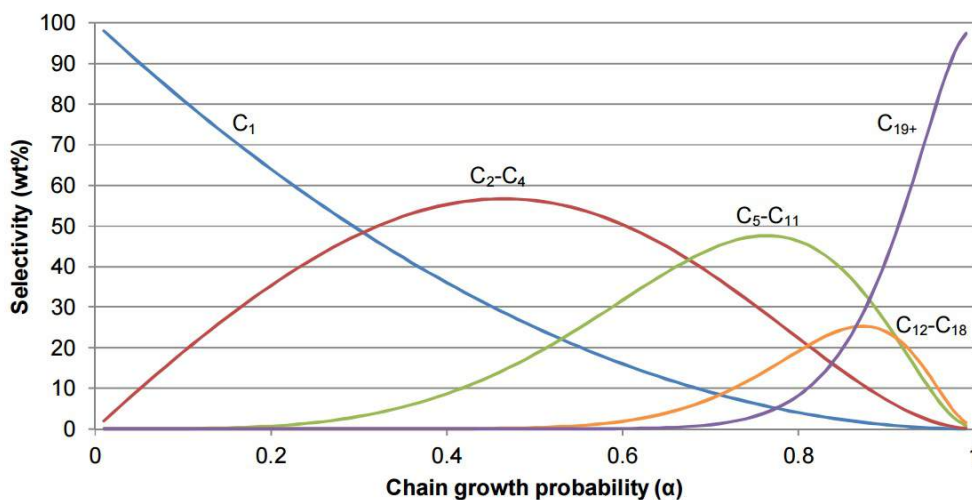
Figure 1.1: The calculated Anderson-Schultz-Flory distribution of Fischer-Tropsch reactions products, dependent on the chain growth probability. Reproduced from[1]

the carbide mechanism used to form alkanes and alkenes on the catalyst surface [16]. In this mechanism, CO is adsorbed dissociatively on the metallic iron surface, upon which the carbon is incorporated in the surface and it can be used for chain initiation and growth. This surface carbon can also lead to coke formation, which will result in the deactivation of the catalytic surface, as low mechanical stability leads to the breaking of the surface[17].

Another metal often used in FT synthesis is cobalt. Cobalt shows high stability and higher productivity at high conversion.[13] It is not as cheap as iron, yet still comparatively cheap, to for example Ru, and possesses a low water-gas shift activity.[13] This is relevant when considering what type of syngas to use: the use of cobalt complements the use of H_2 rich syngas and iron functions better with H_2 poor syngas, as iron possesses a high water-gas shift activity.[13] As natural gas is predominantly used as the source for syngas production in first world countries, cobalt is preferred as FT catalyst.

Cobalt is often utilised as a catalyst for the production of alkanes and alkenes with an, on average, longer chain length (C_{5+}). The focus of this research, however, is on lower olefins. In order to alter the average chain length of the products at industrially relevant conditions (i.e. elevated temperature and pressure), the alpha value of the cobalt catalyst must be driven down. As mentioned previously, measures can be undertaken to direct the selectivity of the FT process, e.g. by the variation of the reaction temperature and/or pressure, the gas hourly space velocity (GHSV), CO/H_2 ratio and the addition of promoters. In general, the effects of reaction conditions on the distribution of FT products can be described. Table 1.1 shows a summary of the general effects of various reaction conditions.[18, 19]

Table 1.1: Effect of reaction conditions on average FT product chain length determined by the chain growth probability, α.

Increase in ...	Effect on α
Temperature	Decrease
Pressure	Increase
GHSV	Decrease
CO:H$_2$ ratio	Increase

The effect of promoter addition is not as straightforward to describe: each promoter can have an individual effect.[20, 21] Promoters can be divided into three classes: structural, electronic and synergistic promoters. Table 1.2 shows examples of these promotion classes and potential elements with these effects (on cobalt).[21]

Table 1.2: Overview of the possible effects of promoters on the functionality of cobalt as a FTS catalyst. Reproduced from [21].

Promotion type	Promotion mode	Influence on catalyst			Element reported in literature to play a role in this promotion effect
		activity	selectivity	stability	
Structural	Support stabilisation	+		+	Mg, Si, Zr, Nb, Rh, La, Ta, Re, Pt
	Cobalt glueing	+		+	B, Mg, Zr
	Cobalt dispersion increase	+		+	Ti, Cr, Mn, Zr, Mo, Ru, Rh, Pd, Ce, Re, Ir, Pt, Th
Electronic	Decorating cobalt surface	+	+	+	B, Mg, K, Ti, V, Cr, Mn, Zr, Mo, La, Ce, Gd, Th
	Cobalt alloying	+	+	+	Ni, Cu, Ru, Pd, Ir, Pt, Re
Synergistic	Water-gas shift	+	+		B, Mn, Cu, Ce
	Hydrogenation / dehydrogenation		+		nr
	Coke burning			+	Ni, Zr, Gd
	H$_2$S adsorption			+	B, Mn, Zn, Zr, Mo

This table underlines that the use of promoters can lead to various effects, sometimes one promoter can have several effects on the FT catalyst. It is therefore unsurprising that the use of promoters on FT catalysts is a field of intense research.

1.1   Research goal

Previous research suggests that high loadings of manganese oxide can be applied as a promoter for cobalt to shift the selectivity towards lower olefins.[22, 19, 23] By promoting Co with MnO, one retains the advantageous aspects of cobalt, i.e. stability and high productivity at high conversion, and combines it with the preferred selectivity, potentially making it a very attractive option for FTO catalysis compared to iron, which deactivates relatively quick and shows a lower productivity at high conversion.[13] However, it is not yet understood what the effect of MnO is on a cobalt catalyst and what interaction causes the shift of the selectivity from long hydrocarbon chains to lower olefins.

The aim is to systematically investigate the enhancement of product selectivity towards lower olefins using cobalt catalysts. To this end several cobalt catalysts, promoted with MnO, for FTO were synthesised and described in this work. Initially, a CoMnO co-precipitated reference system was made. This is a common reference system for Fischer-Tropsch reactions using mixed cobalt/manganese compounds.[22, 19, 23, 13] Co-precipitated CoMnO is a mixed, disordered, bulk compound. It shows the effect of promotion with MnO, however does not provide a system for systematic analysis. The bulk co-precipitated catalysts were used to provide reference boundaries for a model system to be compared with and were therefore used for the determination of reference values for activity and selectivity, as well as for the optimisation of reaction conditions in FTO catalytic testing in terms of temperature and pressure.

Secondly, an attempt was made to synthesise a model catalyst: colloidal CoMnO particles. Colloidal synthesis was used as this method is known to be able to controllably yield well defined, monodisperse particles and allows for the synthesis of an intricately connected bimetallic catalyst. This model system was made to study the effect of MnO on Co as a FTO catalyst. Both types of CoMnO compounds were analysed and used for catalytic testing.

A large part of the performed research focusses on the controlled synthesis of a model CoMnO catalyst, which is required to be well defined in terms of size, shape and composition, as well as being uniform in composition. In the colloidal synthesis, efforts have been made to establish clear guidelines for the synthesis of reproducible model particles. Key to understanding the effect of varying synthesis parameters, is to analyse the synthesised catalysts prior to catalytic testing. Techniques such as electron microscopy (TEM, STEM-EDX, SEM), XRD and XPS were used to this end.

Outline   In this work the performed research is presented in the following way: **Chapter 2** gives a theoretical background relevant for this research topic. **Chapter 3** describes the experimental procedures used for the synthesis, characterisation and catalytic testing of the catalysts. **Chapter 4** and **Chapter 5** encompass the characterisation and performance of the reference and the model catalyst, respectively. **Chapter 6** will compare both the structure and the performance of the reference and the model catalysts, as well as compare multiple colloidal systems with each other and with catalysts described in literature. The chapter will give an extensive discussion on the effects of parameters on and of the synthesis of the various CoMnO systems. From this discussion, a conclusion will be drawn and will be outlined together with the outlook in **Chapter 7**. Additional data can be found in the **Appendix**.

2

Theoretical background

2.1 Fischer-Tropsch synthesis

Fischer-Tropsch mechanism Several mechanisms have been suggested throughout the years for the FT reaction (on cobalt). The consensus is currently that the formation of hydrocarbons in FT reactions occur through the CO insertion mechanism. [24, 25, 26, 27] Figure 2.1 shows a simplified schematic of a number of steps occurring on a catalytic surface during FT synthesis. This is also described in the elemental steps given below.
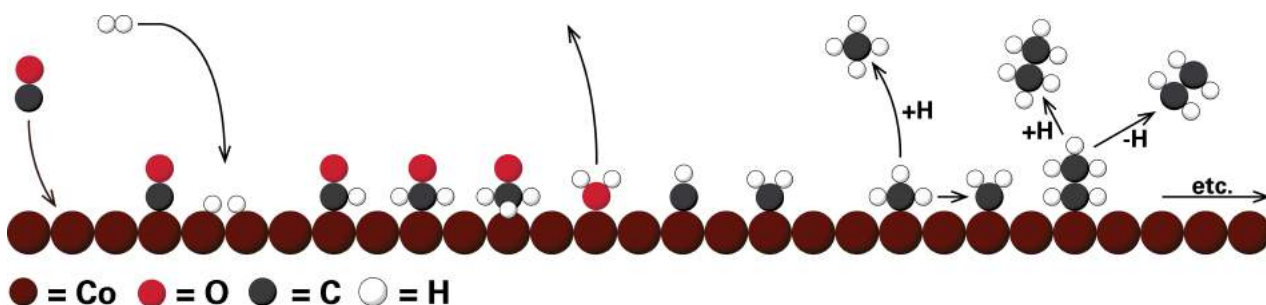

Figure 2.1: The simplified mechanism of hydrocarbon formation on the surface of a cobalt catalyst. The (dissociative) adsorption of reactants, monomer formation, chain growth and desorption are described.

$$CO + * \rightarrow CO^* \tag{2.1}$$

$$H_2 + 2* \rightarrow 2H^* \tag{2.2}$$

$$CO^* + H^* \rightarrow HCO^* + * \tag{2.3}$$

$$HCO^* + H^* \rightarrow H_2CO^* + * \tag{2.4}$$

$$H_2CO^* + H^* \rightarrow H_3CO^* + * \tag{2.5}$$

$$H_3CO^* \rightarrow CH^* + H_2O \tag{2.6}$$

$$CH^* + xH^* \rightarrow CH_x^* \tag{2.7}$$

$$CH_3{}^* + CH_2{}^* \rightarrow CH_2CH_3{}^* + * \tag{2.8}$$

9

$$C_nH_{2n+1}{}^* - H^* \rightarrow C_nH_{2n} + H^* + * \tag{2.9}$$

$$C_nH_{2n+1}{}^* + H^* \rightarrow C_nH_{2n+2} + 2* \tag{2.10}$$
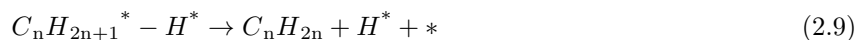
In the mechanism, CO is adsorbed onto the catalyst surface. The CO is then dissociated through hydrogen adsorption, i.e. hydrogen assisted CO dissociation. The absorbed species are further hydrogenated prior to dissociation in OH and CH, the monomer for chain growth, which is further hydrogenated to -CH_3. This mechanism is preferred over the direct dissociation of CO, because of the high activation barrier for direct dissociation.[28, 29, 30, 31, 32] This mechanism has been confirmed by DFT and SSITKA data. [26, 33, 34] Chain propagation occurs via the addition of CH_2 monomers up to the moment of chain termination and desorption of the hydrocarbon chain. The desorption can take place either through H elimination, forming an olefin, or through hydrogenation, forming a paraffin. [35, 36, 37]

The described mechanism is a simplified version of the mechanism. For example, it is well known that not all (surface) sites of a catalyst are equal: the surface of e.g. a metal consists of planes, steps, edges, corners etc.[33] These sites vary in terms of binding energy due to the interaction with their (possibly absent) neighbouring atoms. It is therefore expected that there are preferred sites for the adsorption of CO and H_2. Similarly, preferred bond/product formation sites are present on the surface. Many modelling studies are working on tackling the full mechanism on "real" surfaces with unequal surface sites, defects etc. For example, in the case of cobalt it has been found that adsorption of CO preferentially takes place on step sites, rather than on terraces. Similarly, it has been found that the preferred crystal structure of metallic cobalt for FT reactions is hcp, rather than fcc structure. [38, 26, 24]

2.1.1   Supporting Co catalysts

The activity of cobalt after prolonged time on stream declines due to various effects, such as deactivation through oxide formation caused by water formed in the water-gas shift reaction or due to particle size growth.[39, 40, 10, 41] By supporting catalysts particles, a loss in activity due to particle size growth can be deferred. Simultaneously, by stabilising the (metallic) cobalt particles, the dispersion of the cobalt is increased, thus exposing more surface area per gram of cobalt, i.e. increasing the activity per gram of catalyst (to a certain limit). Therefore, cobalt species are often anchored on (oxidic) supports, such as SiO_2, AlO_2, TiO_2, CNT, etc. [13, 42, 43, 44, 45, 46, 47, 48] Several preparation methods are known to be used, such as homogeneous deposition precipitation (HDP), the sol-gel method, etc., yet the method used most often is incipient wetness impregnation (IWI)[13, 49, 50, 51].

Catalyst-support interaction   Apart from positive support effects, negative effects can also arise. If the interaction between the support and the catalyst species is strong, such as on metal oxide supports, strong metal support interaction (SMSI) effects can occur and mixed cobalt oxide species will form.[39] This can severely decrease the reducibility of the present cobalt species. If the reduction of cobalt oxide is retarded to a large extent, either the active metallic species will be formed at high temperatures only, increasing the change of sintering during reduction procedures, or the reduction procedure will be insufficient to fully reduce the cobalt species to cobalt metal, thereby decreasing the activity.

Additionally, SMSI can cause the oxidic support to cover the cobalt species, thereby shielding the cobalt surface from incoming reactants, thus effectively killing the activity.[13, 21] Combining years of research re-

sulted in the following order in activity found for cobalt on oxidic supports in FT reactions: $Co/TiO_2 >$ $Co/AlO_2 > Co/SiO_2 > Co > Co/MgO$.[13] Additionally, as the interactions are not be purely structural, but can also be electronic in their nature, the supports can also influence on the selectivity of the catalyst.

Supports with significantly less electronic interaction with the cobalt species, are carbonaceous supports, such as CNT, CNF and HSAG. These supports shows sufficient interaction to anchor the cobalt to the surface, thereby increasing the dispersion of cobalt, yet do not interact strongly enough to influence to activity and/or selectivity.

Incipient wetness impregnation   To produce an IWI cobalt catalyst, a porous support (e.g. SiO_2, AlO_2, TiO_2, CNT) is impregnated with a cobalt species solution (e.g. cobalt nitrate) to such an extent that the pores are exactly filled. By varying the concentration of this impregnation solution and/or repeating the procedure, one can effectively vary the loading of the Co/support system. This system is then dried, calcined and reduced. The drying is necessary to expel all solvent, during calcination the cobalt oxide is formed which is subsequently reduced to metallic cobalt; the active phase in FT reactions.

During the drying, calcination and reduction steps, the cobalt species can redistribute over the support surface to an extent dependent on the interaction strength between the cobalt species and the support. Several reports have proposed methods to prevent this redistribution of cobalt, e.g. by variation of drying temperature or environment (air, N_2).[49, 52] Also by varying synthesis parameters, one can control not only the dispersion, but also the particle size.[53, 54] By varying this particle size, several properties have been uncovered, such as an optimum in Co particle size. As FT is a surface polymerisation reaction, the increase of the number of Co surface sites will lead to an increase in activity per gram of catalyst. However, this trend is only valid up to a limit of approximately 7 nm. [55, 53]

2.1.2   Colloidal Co catalyst

The IWI system is a very useful system to study various effects such as loading, reaction conditions, etc. However, it is difficult to exercise control over the system, i.e. synthesise mono-disperse particles. A method to yield a highly ordered system of separate particles with tunable particle sizes and a narrow particle size distribution, is synthesising colloidal particles. A typical colloidal synthesis is described in the polyol process. [56, 57] In this process, a cobalt precursor solution (e.g. cobaltcarbonyl) is added to a boiling alcohol (e.g. 1,2-hexadecanediol) in which stabilising surfactants are present (e.g. oleic acid, oleylamine). These surfactants are necessary as the synthesised cobalt particles will instantaneously aggregate into large cobalt clusters when synthesised in absence of these surfactants. By adapting the ratio of cobalt precursor and surfactants, one can vary the particle size of the colloidal particles. These colloids can subsequently be deposited on a support if desired.

2.1.3   Performance Co catalysts

To provide a window of reference, some Co-based systems described in literature will be used to compare the activity and selectivity of the catalysts produced in this work. The literature reference systems have been selected by their method of preparation and testing, i.e. a standard IWI system and a colloidal system are
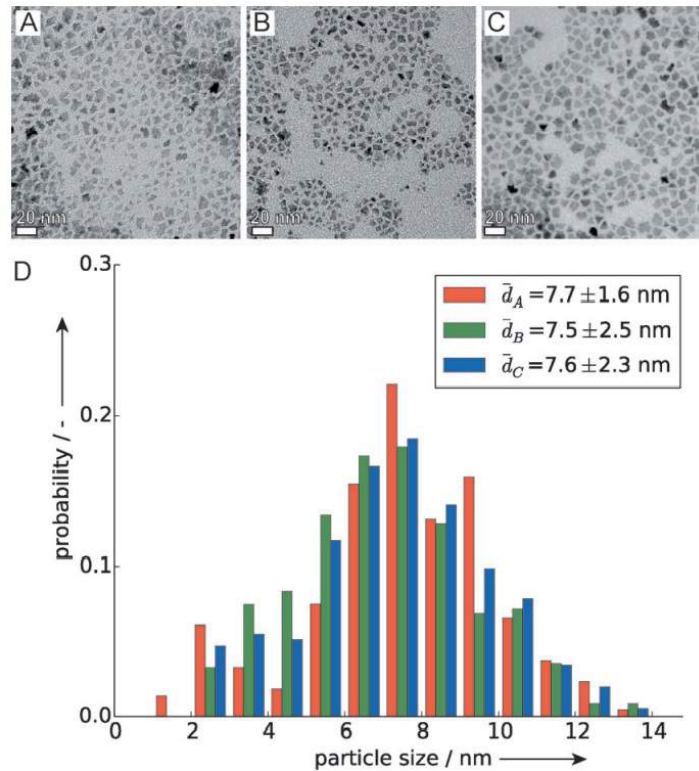
Figure 2.2: **A-C**:3 TEM images of colloidal cobalt particles, **D:** the particle size distribution of these colloidal samples. Reproduced from [57]

desired for comparison, and naturally it is preferred that these system are tested for FT activity and selectivity in a manner similar to the method described in this work. Therefore, an IWI Co/CNT catalyst will be used, as CNTs show little metal-support interaction and for the unsupported colloids produced in this work, SMSI is also absent[58]. Additionally, a colloidal Co/SiO_2 catalyst is used as literature reference. [57] Figure 2.3 shows TEM images of three batches of these colloidal particles, together with their particle size distribution.

Figure 2.3 shows a low pressure (1 bar) measurement of Co/CNT particles, synthesised through IWI[58]. The following selectivities were obtained (TOS=13 hours): 42%, 28% and 30% for the C_1, C_2-C_4 and C_{5+} fractions, respectively. This corresponding activity (in CTY) is $3.8*10^{-5}$mol CO/g_{Co}/s.
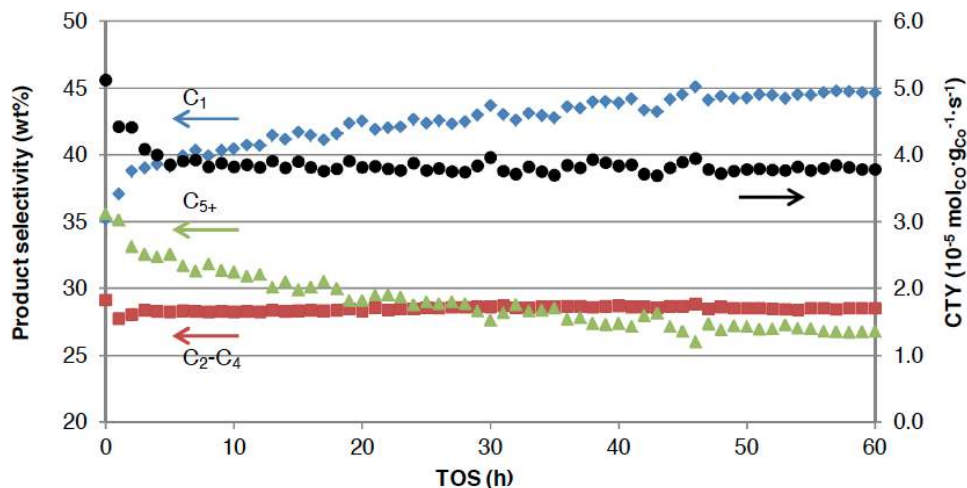
Figure 2.3: The performance of 10 wt%Co/CNT particles prepared through IWI in terms of activity (cobalt time yield (CTY))and selectivity. Results obtained at 220 °C, 1 bar, GHSV=4000h^{-1}, H$_2$:CO=2, reproduced from [58].

Figure 2.4 shows the performance of SiO$_2$ supported cobalt colloidal particles (7.5 nm) together with Co/SiO$_2$ particles prepared through IWI. The performance of Co colloids/SiO$_2$ as well as CoMn colloids/SiO$_2$ is shown in Figure 2.4. The CoMn particles will be discussed further in the subsection **Co as FTO catalyst**.
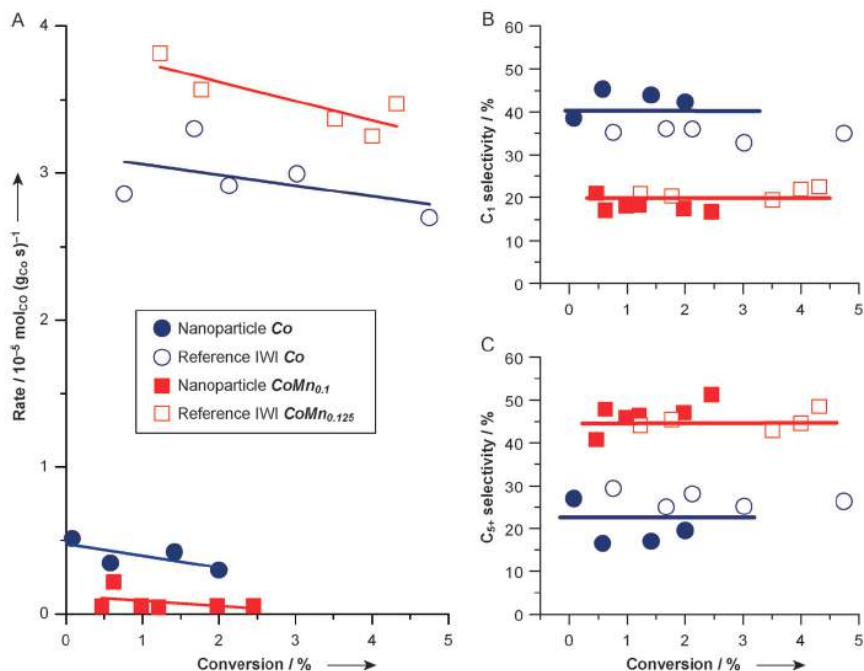
Figure 2.4: The performance of colloidal Co particles in comparison to IWI Co particles in terms of activity and selectivity. Both colloidal and IWI particles are supported on SiO_2. Also present in this figure is data on Mn promoted Co particles. The activity is given in terms of cobalt time yield, this data was obtained at $220\,^\circ C$ and 1 bar, reproduced from [57].

The figure clearly illustrates the similarities and differences between the two systems: the IWI- and colloidal system show a remarkably similar selectivity and a large difference in activity. The shown selectivities for both catalysts are similar to the selectivity shown for the Co/CNT catalyst, see Table 2.1. The reported selectivity is at a CO conversion of 1-2% for the colloidal and Co/SiO_2 systems. As the CO conversion can be of influence on the selectivity of a catalyst, a CO conversion of 1-2% is typically aimed for to compare catalysts.

Table 2.1: Selectivity of several supported cobalt catalysts reported in literature. These selectivities were achieved at $220\,^\circ C$, 1 bar, H_2:CO=2.

	Selectivity (%)		
Catalyst ID	$\mathbf{C_1}$	$\mathbf{C_2\text{-}C_4}$	$\mathbf{C_{5+}}$
Co/CNT[58]	42	28	30
$\mathbf{Co/SiO_2}$ (IWI)[57]	35	40	25
$\mathbf{Co/SiO_2}$(Colloidal)[57]	44	41	15

Even though Co catalysts are typically used as high alpha FTS catalysts for the production of C_{5+} hydrocarbons, one can see that the C_{5+} fraction is not the largest fraction for either of these catalysts. This can be expected, as industrial FTS processes are executed a high pressures (20 bar or higher), thus driving the selectivity towards C_{5+}. However, this is a useful set of references to study the effect of promoter addition and its effect on the selectivity (and activity).

14

2.2   Fe as FTO catalyst

Iron is an element often used for Fischer-Tropsch reactions as it is a cheap material with a high activity and a very high water-gas shift activity, making it especially suitable for H_2 poor syngas conversions, e.g. syngas synthesised from a coal feed. Next to high alpha reactions, iron can also be used as a low alpha ($\sim$0.5) catalyst at industrially relevant conditions (i.e. elevated temperature and pressure), thereby having the propensity to produce a product distribution with a large C_2-C_4 fraction. Additionally, as Fe possesses a low hydrogenation activity, this fraction has a largely olefinic character, therefore Fe is a good Fischer-Tropsch to olefins (FTO) catalyst.[1]

Again, many Fe-based catalytic systems are known, as is the case for Co, such as IWI, HDP, co-precipitated and colloidal systems. A colloidal iron FTO catalyst will briefly be discussed, mainly as Fe is a good reference for the study of the FTO capacities of Co, as well as the fact that the synthesis procedure of these iron colloidal particles provided an initial outline for the colloidal cobalt particle synthesis.

2.2.1   Fe colloidal catalyst

A recent article by Casavola et al. described the synthesis of colloidal iron(oxide) particles and their deposition on CNTs.[15] Figure 2.5 shows TEM images of six colloidal samples of varied average particle size.
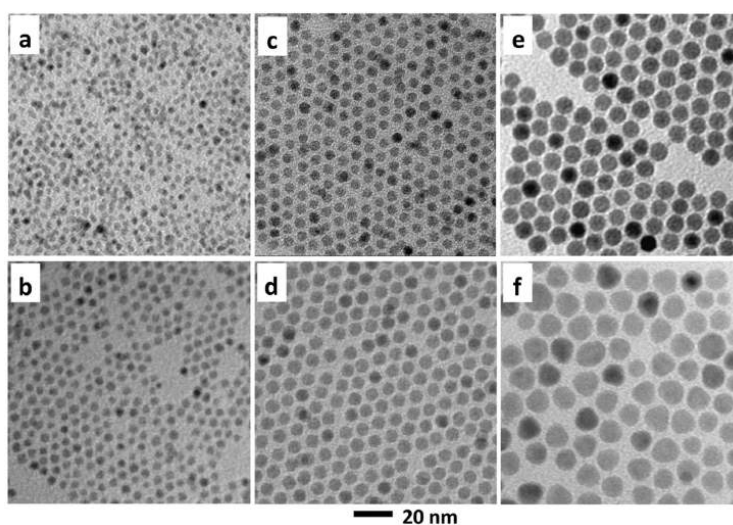

Figure 2.5: **A-F:** TEM images of iron oxide colloidal particles of various sizes, reproduced from [15].

These particles were synthesised through the polyol process with a narrow size distribution. The 7 nm colloids deposited on CNT were used for FTO catalytic testing (1 bar, 350 °C, H_2:CO=1). The activity is given as the iron time yield (FTY). At a FTY of $0.19 \ast 10^{-5}$ mol CO/g_{Fe}/s (TOS=15 hours) a selectivity of 31%, 60% and 7% was found for the methane, lower olefin and C_{5+} fraction, respectively (α =0.43).

Disadvantages of iron

Iron is a potent FTO catalyst, yet possesses flaws: it tends to deactivate relatively quickly if one compares it, for example, with cobalt. [41, 59] Additionally, Fe is a very well-functioning catalyst in a H_2 poor syngas feed. However, currently a trend is present in moving away from the use of coal in favour of the use of e.g. natural-, or in the future, shale gas, two feeds which yield a H_2 rich syngas. Because of this, a high water-gas shift activity is undesired.

2.3   MnO as promoter in FTS/FTO

The use of MnO as a promoter, as is done in this work, is not new: many papers have been published of the use of MnO as a promoter for the suppression of methane production. [60, 61, 62, 63, 64, 65] In these researches, the MnO is deposited in close proximity to the active phase and can show an electronic (and/or structural) interaction with the catalytically active species. To achieve this promoting effect, as little as a few weightpercent loading is required.

This effect is visible in Figure 2.4: it clearly shows that the production of methane is lower for the CoMn particles in comparison to the Co particles, resulting in a larger C_{5+} fraction, due to a shift in the catalyst' alpha value. Additionally, when promoting with Mn in an IWI system, the activity increases, however, the opposite is true for the colloidal particles. Small loadings of Mn are known to have a positive electronic effect on the Co activity. [61, 62, 57, 60, 64] However, the observed lowering in activity of the colloidal particles may be an effect of the covering of the available colloidal Co surface with Mn. This effect may be absent for the CoMn/SiO$_2$(IWI) system as the particles were produced through subsequent impregnation steps and the Mn may be stabilised on the surface of the support close to the Co, rather than on the Co surface (SMSI). The colloidal CoMn particles are also stabilised on SiO$_2$, yet the CoMn colloids were synthesised prior to stabilisation, thereby depositing the Mn on Co. Additionally, the article described that sintering may have influenced the observed activity.

2.3.1   Co as FTO catalyst

A drastically different case is the promotion of cobalt with large amounts of MnO (up to 80 wt%) to produce a FTO catalyst.[22, 19, 23] A recent article by Zhou et al. has focussed on using MnO as a promoter to synthesise a cobalt-based FTO catalyst.[22] In this article they described the synthesis of a co-precipitated CoMnO catalyst through the co-precipitation of cobalt- and manganese nitrate in either water or 1,4-butadienediol. (Figure 2.6)

They found that both these catalysts had a large selectivity towards the C_2-C_4 fraction, as can be seen in Table 2.2.
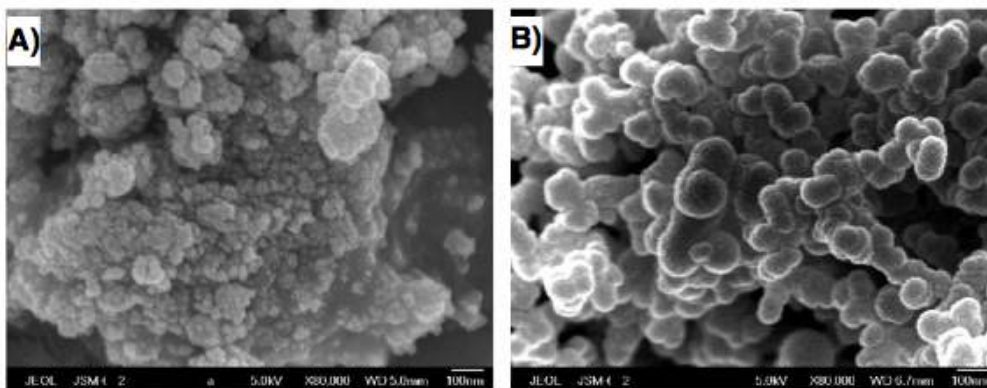
Figure 2.6: SEM images of **A:** Co/MnO_x-H_2O and **B:** Co/MnO_x-BDO. Reproduced from [22].

Table 2.2: The selectivity of two co-precipitated CoMnO catalysts at $240\,°C$ and 1 bar, GHSV=2500 h^{-1}, H_2/CO=2.

Selectivity (%)				
Catalyst ID	**C$_1$**	**C$_2$-C$_4$$^=$**	**C$_2$-C$_4$$^-$**	**C$_{5+}$**
Co/MnO$_x$-H$_2$O	11.0	26.5	26.2	31.7
Co/MnO$_x$-BDO	9.1	42.2	17.7	30.4

It becomes clear that one catalyst shows more FTO catalyst behaviour than the other: for Co/MnO_x-BDO, the main products are lower olefins, whereas Co/MnO_x-H_2O also gives as a main fraction the C_2-C_4 fraction, however, with a O/P ratio of 1.01, thus yielding less olefinic hydrocarbons. The low methane selectivity, a characteristic accredited to MnO, may also be attributed to the low GHSV used for these measurements, resulting in a high conversion (42-45%). If one, for example, compares these catalysts to the previously outlined Co catalysts (Table 2.1), one sees a very large drop in methane selectivity upon addition of (a large quantity of) MnO. Unfortunately, the O/P ratios for the C_2-C_4 fraction is not known for the supported pure cobalt catalysts, therefore, little can be said about the potential FTO properties of these catalysts. Nonetheless, the co-precipitation of Co and MnO seems to be an effective manner to synthesise a catalyst with a relatively high lower olefin selectivity for a cobalt catalyst.

3

Experimental procedure

3.1 Catalyst preparation

3.1.1 Bulk co-precipitated CoMnO

The following chemicals (including purity and brand) were used for the synthesis of co-precipitated CoMnO: $Co(NO_3)_2\cdot 6\ H_2O$ (99+%, Acros), $Mn(NO_3)_2\cdot 4\ H_2O$ (97,5+%, Acros), $(NH_4)_2CO_3$ (30+%(NH_3), Acros).

Through the co-precipitation of cobalt- and manganese nitrate -induced by the addition of ammonium carbonate-, bulk CoMnO was synthesised.[22, 19] A schematic overview of the experimental setup is given in Figure 3.1.
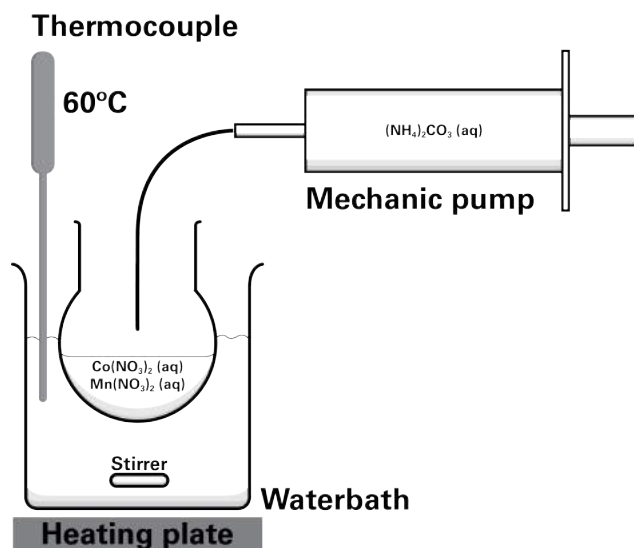

Figure 3.1: Simplified schematic of the experimental setup used for the co-precipitation of CoMnO.

Four samples of bulk CoMnO were synthesised, differing in their Co:MnO weight ratio, their names defined by this ratio [22]. Table 3.1 gives the amount of chemicals used per synthesis. $Co(NO_3)_2\cdot 6\ H_2O$ and $Mn(NO_3)_2\cdot 4\ H_2O$ were dissolved in 40 mL of H_2O at room temperature in a round bottom flask, the

Table 3.1: Amounts of chemicals used for bulk CoMnO syntheses.

Catlyst ID	$Co(NO_3)_2$ $\cdot 6\ H_2O$ (g)	$Mn(NO_3)_2$ $\cdot 4\ H_2O$ (g)	$(NH_4)_2$ $(CO_3)_2$ (g)	H_2O (mL)
Cat 20/80	2.47	5.66	3.84	40
Cat 35/65	4.00	4.25	3.84	40
Cat 50/50	5.50	3.18	3.84	40
Cat 65/35	7.00	2.12	3.84	40

solution was stirred for 1 hour and then placed in a water bath of 60 °C. Co-precipitation was induced by the drop wise addition of 20 mL of 1M $(NH_4)_2CO_3$ solution using a mechanic pump, over a period 20 minutes.

The resulting pink solid was aged for 30 minutes at room temperature, decanted, washed 3 times with approximately 100 mL of water followed by decantation after each washing step. The sample was dried for 2 hours in a static oven at 120 °C, during which period the material was stirred every 30 minutes. The powder was subsequently calcined in flowing air at 400 °C for 2 hours with a heating rate of 2 °Cmin⁻¹.

3.1.2 Model colloidal CoMnO

The following chemicals (including purity and supplier) were used for the synthesis of colloidal CoMnO: $Co_2(CO)_8$ (95%, Acros), $Mn_2(CO)_{10}$ (98%, Sigma-Aldrich), 1-octadecene (90%, Aldrich), oleic acid (90%, Aldrich), 1,2-hexadecanediol (90%, Aldrich), oleylamine (70%, Aldrich), toluene (99.8%, Acros) and 2-propanol (99.5%, Sigma-Aldrich).

The colloidal CoMnO particles were synthesized using the polyol process [15]. A 50 mL round bottom flask with 1.2 mmol of 1.2-hexadecanediol, 0.75 mmol of oleylamine, 1.5 mmol oleic acid, 10 mL of 1-octadecene and a magnetic stirrer was placed in the heating mantle seen in Figure 3.2, with the thermocouple placed between the flask and heating mantle. The flask was connected to the Schlenk line through a cooler and a t-splitter valve, while the other two necks were closed with a white septum.
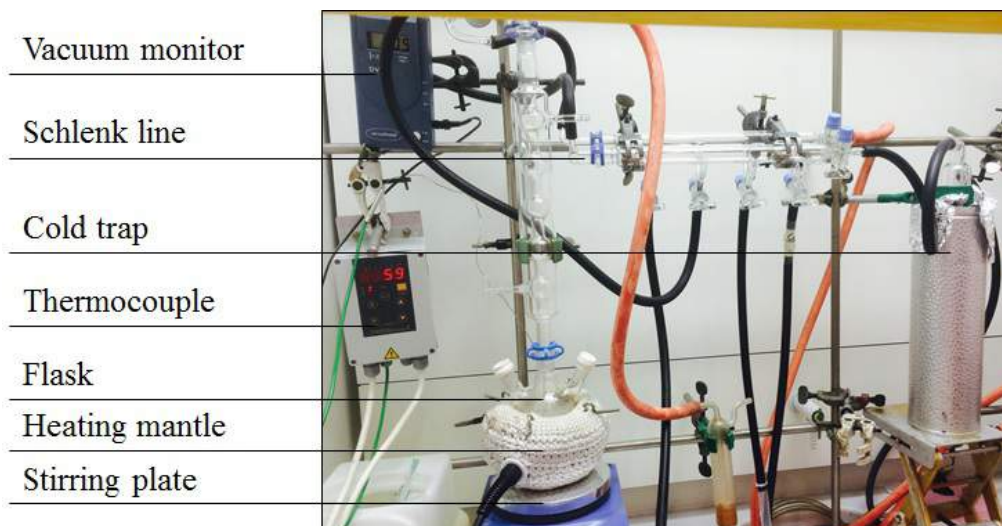
Figure 3.2: Picture of the experimental setup used for colloidal synthesis.

The flask was heated with the highest possible heating rate to 120 °C whilst stirring at 650 rpm. During the heating, the flask was placed under vacuum at 110 °C. The system was kept at 120 °C for one hour. Simultaneously, 0.2 mmol of $Co_2(CO)_8$ and 0.8 mmol of $Mn_2(CO)_{10}$ were dissolved in 3.5 mL of 1-octadecene in a glass vial (7 mL, piercable teflon lined cap) in a glovebox. The solution was heated for 30 minutes using a heating plate set at 45 °C and was shaken. The flask was flushed with N_2 three times, placed under N_2-flow and lifted from the heating mantle after which the thermocouple was placed in the flask reaction mixture by piercing a septum. At a surfactant solution temperature of 90 °C, the metal precursor solution was added through hot injection using a syringe and the flask was heated with the highest possible heating rate to 290 °C where it was kept for one hour. During this heating process, vapour formation was visible (Figure 3.3) and the reaction mixture changed colour from yellow to green/grey.

Figure 3.3: Visible vapour formation during the colloidal synthesis.

The flask was cooled to room temperature and exposed to air upon which the colour turned to dark grey, possibly due to the oxidation of metallic cobalt to cobalt oxide. The reaction mixture was transferred fully to two 20 mL glass vials by rinsing the flask with 6 drops of toluene (Pasteur pipette) after transfer. Superfluous organic compounds were removed by washing the colloidal solution thrice with approximately 20 mL of iso-propanol and centrifuging for 10 min at 3700 rpm. After each centrifugation the particles were re-dispersed in 3 drops of toluene (Pasteur pipette). Particles used for TEM analysis were kept in toluene, for other purposes, the vials were opened to air to evaporate the toluene prior to chracaterisation and/or catalytic testing.

The procedure described here was a "standard" colloidal synthesis. Some of the important synthesis parameters were changed throughout the work on colloidal synthesis. To facilitate comparison, this set of standard reaction parameters is given in Table 3.2.

Table 3.2: Set of reaction parameters encompassing a standard colloidal synthesis.

Reaction parameter	Value
Amount 1,2-hexadecanediol	1.2 mmol
Amount oleic acid	1.5 mmol
Amount oleylamine	0.75 mmol
Amount metalprecursor	1 mmol
Ratio metalprecursor	Co:Mn = 20:80
Precursor dissolving volume	3.5 mL
Flask size	50 mL
Injection temperature	90 °C
Final temperature	290 °C
Heating rate	"2"

The standard synthesis initially yielded tripod colloids and yielded tetrahedral particles after a change in $Mn_2(CO)_{10}$ precursor batch. Other "standardised" syntheses (i.e. syntheses used for the synthesis of tetrahedral and hexagonal particles used for analysis and catalytic testing) are summarised in Table 3.3.

Table 3.3: Parameter variations in colloidal synthesis. Changes in parameters are printed in bold.

Reaction parameter	Tetrahedral	Hexagonal
Amount 1,2-hexadecanediol	1.2 mmol	1.2 mmol
Amount oleic acid	1.5 mmol	1.5 mmol
Amount oleylamine	**1.00 mmol**	0.75 mmol
Amount metalprecursor	1 mmol	1 mmol
Ratio metalprecursor	Co:Mn = 20:80	Co:Mn = 20:80
Precursor dissolving volume	3.5 mL	**7 mL**
Flask size	100 mL	100 mL
Injection temperature	90 °C	**140 °C**
Final temperature	290 °C	290 °C
Heating rate	"3"	"3"

3.1.3   Deposition on CNT

The colloidal CoMnO particles could be deposited on CNTs prior to catalytic testing [15]. In this procedure, 5 mL 1-octadecene was added to 20 mg of colloidal particles which were dispersed in toluene. 800 mg of CNTs of the sieve fraction 215-425 μm were added to a 50 mL threenecked flask and dispersed in 5 mL of 1-octadecene. The colloidal dispersion was added to the flask, together with a magnetic stirrer, which had one neck closed with a septum and one with a stopper. The flask was placed in the same setup as for the colloidal synthesis, with the thermocouple between the flask and heating mantle, and was placed under vacuum to boil the toluene out at 120 °C. The flask was left to stir for 15 min before it was flushed with nitrogen 3 times and placed under N_2 flow. The thermocouple was then placed in the flask by piercing the septum, after which the flask was heated at 300 °C for 30 minutes (highest possible heating rate). The flask was then cooled to room temperature and washed with n-hexane and acetone. The solvents were added in a hexane:acetone ratio of 1:3. The n-hexane was added prior to the acetone and after the addition of the solvents the flask was decanted. This washing procedure was repeated 5 times. Subsequently, the residue was dried in a static oven for 1 hour at 60 °C, 3 hours at 120 °C and 3 hours under vacuum at 80 °C.

3.2   Characterisation

3.2.1   SEM

SEM images were made using a JEOL Neoscope II JCM-6000. Prior to analysis, the samples were deposited on a carbon film placed on a SEM holder.

3.2.2   TEM

Each of the prepared colloidal samples was characterised with TEM using a Philips FEI Tecnai-10 (100kV) or a Philips FEI Technai-20 FEG (200kV). The colloidal particles were dispersed in a small amount of toluene, sonicated shortly and drop casted on Formvar/Carbon Films with 300 Mesh copper (50). Analysis of the TEM images was performed using iTem software, e.g. for the determination of particle size distribution calculations.

STEM-EDX

For STEM-EDX analysis, samples were ground, dissolved in toluene, shortly sonicated and drop-casted on Formvar/Carbon Films with 300 Mesh copper (50). HAADF images were made using a FEI Talos F200X microscope. EDX analysis was performed using a high-brightness field emission gun (X-FEG) and a Super-X G2 EDX detector. Using Velox software, EDX maps of the colloidal particles were made.

3.2.3   XRD

Bulk CoMnO

XRD measurements were performed using a Bruker-AXS D2 Phaser equipped with a Co Kα radiation ($\lambda = 1,78897$ Å) source with 2θ from $20 - 80°$, using an increment of 0.18, with a step measurement time of 2 s. The detector lower discriminator was set at 0.11 to quench the measured fluorescence. The samples were

placed in a deep silicon holder. All samples were measured for 4 hours on autorepeat to enhance the S/N ratio. Analysis of the results (crystal structure fit, crystallite size calculations, etc.) was performed using EVA software.

Colloidal particles

The samples were measured with Bruker D8 Discover in transmission capillary geometry with Mo ($K_{\alpha 1} =$ 0.709 nm) source and 980 μm inner diameter capillaries (1000 μm outer diameter). Samples were mixed with amorphous SiO_2(Aerosil OX50, 212-425 m) in approximate mass ratio of 2:1 (SiO_2:Sample) i.e. about 14 mg of diluent to 7 mg of sample. Dilution was done to prevent excessive mass absorption by the dense sample material and to spread the sample material over the whole ($\sim$18 mm) beam length. Measurement parameters used were the 2θ range of $5 - 55\,^\circ$ with step size of 0.0358 and exposure time of 40s per step. The Mo source was ran with power of 2500 W (50 kV x 50 mA).

Rietveld Analysis on measured samples was done using TOPAS 5 software package. Fitting was done with structures found for $Mn_xCo_yO_4$ alloys from the PDF-4+ 2015 database. Fitting with structures for Co and Mn oxides was also attempted but no fitting combinations were found i.e. all/most crystalline material was in form of $Mn_xCo_yO_4$ alloys and those structures were therefore used for fitting. Default structures from the database were refined further to match the experimental diffractograms. An individual peak was used to fit the amorphous peak resulting from the SiO_2 diluent and rest of the background was corrected with software provided polynomial. Sample displacement and absorption path length error in capillary geometry were corrected with software provided functions. None of the default $Mn_xCo_yO_4$ structures fitted precisely on the measured diffractograms, this is presumably due to differing Mn:Co ratios on the experimental alloys vs. the default database structures. Therefore the lattice parameters of the most closely fitting default structures were refined to fit the experimental diffractograms. The Mn:Co ratio of the refined structures were estimated from a function fitted to the database structures per crystal symmetry.

3.2.4   TPR

A Micromeritics Autochem 2920 apparatus was used for TPR measurements, using a ramp of $5\,^\circ$Cmin^{-1} up to $750\,^\circ$C, under a 50 mLmin^{-1} flow of 5% H_2/Ar. For a typical measurement, 50 mg of bulk- and 20 mg of colloidal catalyst (the full amount produced per synthesis) was used, where extra precaution had to be taken for the securing of the model catalyst between two amounts of glass wool in order to prevent leakage of the catalyst into the instrument. A TCD detector measured the amount of gas uptake, results were normalised per gram of sample.

3.2.5   XPS

XPS spectra were acquired on a Thermo Scientific K-Alpha spectrometer using a Al K (h = 1486.6 eV) monochromatic small-spot X-ray source. Charging effects were corrected by using the adventitious carbon C1s (sp^3) peak as reference for all samples at a binding energy (BE) of 284.8 eV. Fitting of the spectra (BE, FWHM, peak shape, asymmetry, number of species) was performed with CasaXPS software, version 2.3.16.

3.3   Catalytic testing

3.3.1   Low pressure testing

In low pressure testing, a glass plug-flow reactor was loaded with 20 mg of catalyst, diluted with 200 mg of SiC of a particle sieve fraction of 215-425 micrometers to prevent hot-spots and mass transfer limitations during testing. The testing procedure is visualised in Figure 3.4. An in-situ reduction at 350 °C (heating in He-flow, rate=5 °Cmin^{-1}) in a mixed He:H$_2$ flow was followed by catalytic testing at 240 °C (cooling in He-flow, rate=2 °Cmin^{-1}) in a syngas flow with a H$_2$:CO ratio of 2. A typical test ran for 24 hours, with a syngas flow of 6:3 mLmin^{-1}. Using an online GC (Varian CP3800 analyzer, FID detector, CP Sil 5 CB column) a product stream sample was taken every hour. From the GC data, the CO conversion and selectivity could be calculated by integrating the peaks in the gas chromatograms with CP-Maitre Elite software.
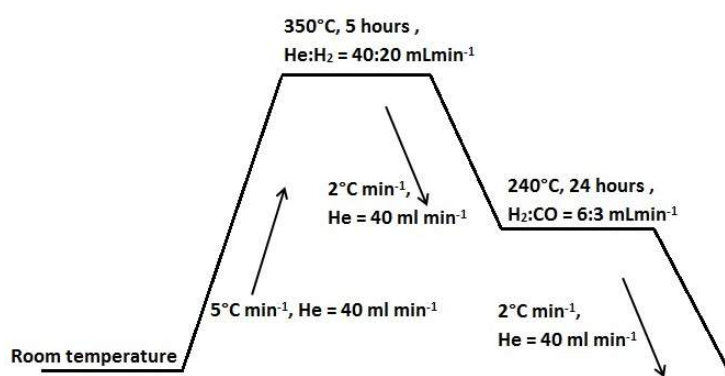

Figure 3.4: Experimental procedure for low pressure catalytic testing.

3.3.2   High pressure testing (Flowrence)

A high pressure catalytic test was performed in an Avantium 16 parallel reactor setup (Flowrence) equipped with an online Agilent Technologies 7890Q GC. Hydrocarbon streams were separated on an Agilent J&W PoraBond Q column and detected using a FID detector, carrier gases were separated on a micropacked Shin-Carbon ST column and analysed using a TCD detector. Several reactors were loaded with 50 μL of each of the co-precipitated catalysts mixed together with 100 μL of SiC of a particle size range of 215-425 μm. Additionally, another 3 reactors were loaded with varying amounts (50, 100 or 150 μL) of Cat 20/80, the catalyst which is expected to behave as the best FTO catalyst out of the 4 co-precipitated samples [22], and 2 reactors with approximately 20 mg of colloidal catalyst (tripods). These stated amounts of catalyst were diluted with SiC to such an extent that the total height of the sample bed was constant throughout the multiple reactors ($\sim$3.5 cm). The testing procedure was comparable to the low pressure procedure. An in-situ reduction at 350 °C in H$_2$-flow (heating rate=5 °Cmin^{-1}) was followed by catalytic testing (cooling rate=2 °Cmin^{-1}) in syngas flow (H$_2$:CO=2). During the test, several reaction condition variations were applied to the samples: temperatures of 220, 240, 260, 280 °C at 10 bar and pressures of 5, 10, 15 and 20 bar at 240 °C [19]. Table 3.4 gives a summary of all FTO testing conditions for both low and high pressure testing.

Table 3.4: Overview of reaction steps and their corresponding conditions used for low and high pressure catalytic testing.

Low pressure (1 bar)			
Reaction step	**Reduction**	**Cooling down /Flushing**	**FTO**
Heating/cooling rate ($^\circ$Cmin^{-1})	5	2	n.a.
Temperature ($^\circ$C)	350	n.a.	240
Gas composition	He:H$_2$	He	H$_2$:CO
Gas flow (mLmin^{-1})	40:20	40	6:3
Time (h)	5	1	24
High pressure (per reactor; at 5, 10, 15 and 20 bar)			
Reaction step	**Reduction**	**Cooling down /Flushing**	**FTO**
Heating/cooling rate ($^\circ$Cmin^{-1})	5	2	n.a.
Temperature ($^\circ$C)	350	n.a.	220/240/260/280
Gas composition	Ar:H$_2$	Ar	H$_2$:CO:Ar
Gas flow (mLmin^{-1})	40:20	40	6:3
Time (h)	5	1	126

3.3.3   Data analysis

The activity of a catalyst can be defined as the cobalt time yield(CTY), i.e. the amount of CO converted per amount of cobalt per time unit. The CO conversion can be calculated in the following two ways:

$$CO\ Conversion(\%) = \frac{\sum n_i M_i}{M_{CO}} \times 100(\%) \tag{3.1}$$

$$CO\ Conversion(\%) = \frac{Q_{in} - Q_{out}}{Q_{in}} \times 100(\%) \tag{3.2}$$

In equation 3.1 where n_i is the number of carbon atoms in product i, M_i is the percentage of product i and M_{CO} is the percentage of CO in the syngas feed, the number of converted carbon atoms is summarised and is divided by the total number of fed carbon atoms. In equation 3.2, where Q_{in} is the volumetric flow of fed CO (mlmin^{-1})and Q_{out} is the volumetric flow of unreacted CO out of the reactor, the amount of reacted CO is divided by the amount of fed CO. When using an gas chromatograph with a thermal conductivity detector, the CO conversion is calculated using equation 3.1, whereas equation 3.2 is used in combination with FID detectors.

Equation 3.3 shows the calculation of the CTY, where χ_{CO} is the CO conversion and m$_{Co}$ is the cobalt mass.

$$CTY(\%) = \frac{Q_{CO} \times \chi_{CO}}{m_{Co}} \tag{3.3}$$

Equation 3.4 shows how the selectivity of a carbon number fraction (S_i) is calculated.

$$S_i(\%) = \frac{n_i M_i}{\sum n_i M_i} \times 100(\%) \tag{3.4}$$

Lastly, the calculation for the gas hourly space velocity (GHSV) is given (equation 3.5), where Q_{flow} is the volumetric flow of the fed syngas (mLmin^{-1}) at standard temperature and pressure, and $V_{catalyst}$ is the volume of the reactor bed (catalyst).

$$GHSV(h^{-1}) = \frac{Q_{flow}(STP)}{V_{catalyst}} \tag{3.5}$$

4

Reference catalyst: co-precipitated CoMnO

4.1 Characterisation

4.1.1 SEM

SEM images of the catalysts are shown in Figure 4.1. Interesting to see is the presence of a combination of surface morphologies: spherical surface elements and layered/square surface elements. Closer inspection of the images showed that the surface composition changes with a change in Co:MnO ratio: the character of the catalyst with the highest Co:MnO ratio was predominantly spherical, whereas the content of layered/square elements increases with a decreasing Co:MnO ratio.

SEM-EDX analysis on the surface of these catalysts showed that per sample, even though the morphology of the surface was incongruent, the chemical composition was consistent throughout the catalysts. It is not known whether or not the diversity in surface morphology has an influence on the activity or selectivity of the catalyst in FTO reactions.
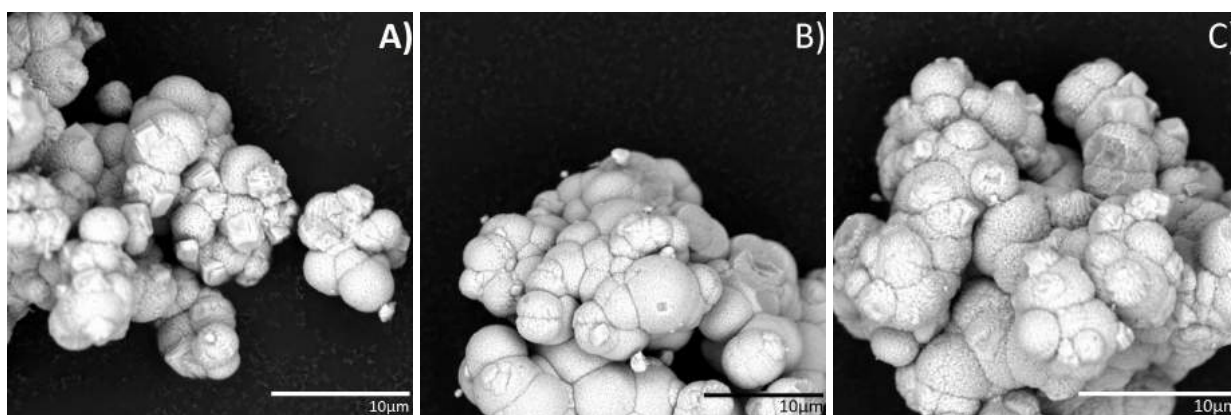

Figure 4.1: SEM images of the co-precipitated CoMnO catalysts with a Co:MnO weight ratio of **A:** 20/80, **B:** 35/65 and **C:** 50/50.
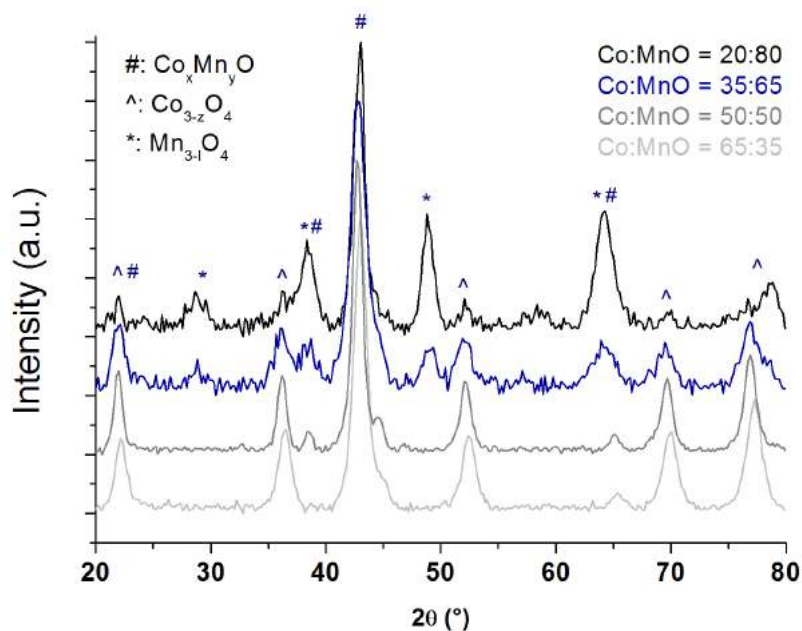
4.1.2 XRD

Figure 4.2: XRD diffractograms of the co-precipitated catalysts. Using the #, ˆ and * symbols, peaks corresponding to different crystal structures are shown for these catalysts.

The XRD diffractograms of the co-precipitated CoMnO samples are shown in Figure 4.2, in which the relevant peaks are indicated. The quality of the diffractograms is unfortunately poor, a phenomenon ascribed to fluorescence of the samples, as a Co source is used and the samples are (variably) high in Mn content. Therefore, the smaller the Mn content of a sample, the better the quality of the XRD diffractogram.

All of the spectra have been fitted with possible CoMnO crystal structures. No definitive fit has been found for any of the catalysts, indicating that these catalysts consist of mixed crystal structures, typically mixed spinel structures. Separate Co and Mn species, indicated with ˆ and *, respectively, are present in varying degrees for the catalysts, i.e. samples high in Mn content possess separate Mn species and no noticeable separate Co species, and vice versa. Accompanying a shift in Co:Mn ratio, is a variation in in the crystallite sizes (Table 4.1). The crystallite sizes have been calculated using the Scherrer equation with a line broadening of 0.1. No clear trend is visible in crystallite sizes for these samples. As these catalysts were not made in duplo, these results may result from experimental errors.

Table 4.1: Crystallite sizes of the co-precipitated catalysts calculated by the Scherrer equation.

Sample ID	$Co_xMn_yO_4$ crystallite size (nm)	$Co_{3-z}O_4$ crystallite size (nm)	$Mn_{3-l}O_4$ crystallite size (nm)
Cat 20/80	11	n.a.	7
Cat 35/65	7	n.a.	n.a.
Cat 50/50	11	12	11
Cat 65/35	8	n.a.	9

4.1.3   TPR

The effect of a high MnO loading on the reducibility of cobalt oxide was tested using TPR. Figure 4.3 shows the reduction behaviour of the bulk CoMnO (Cat 20/80). XRD showed that Cat 20/80 consists of various crystal structures, amongst which the main components are CoMnO spinels and $Mn_{3-l}O_4$. For Co_3O_4, two reduction peaks are expected for the reduction to CoO (240 °C) and to Co metal (340 °C).[60][60] For Mn_3O_4 reduction peaks for the partial reduction to MnO_2 (200 °C) and the direct/indirect reduction to MnO, i.e. Mn_3O_4 and/or MnO_2 to MnO, (430 °C) are expected. [66]
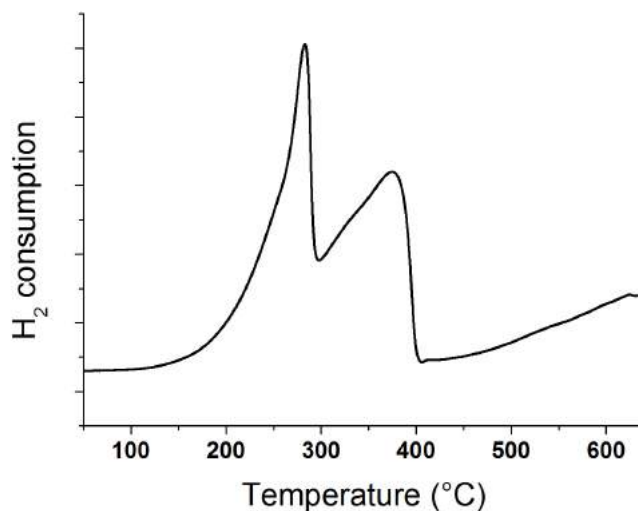

Figure 4.3: TPR spectrum of the reference catalyst.

In the TPR spectrum, two reduction peaks are observed at 270 °C and 470 °C with shoulders at 250 °C and 320 °C. The main reduction peaks are therefore ascribed to the reduction of Co_3O_4 to CoO and the reduction of Mn_3O_4/MnO_2 to MnO, with the first shoulder belonging to the partial reduction of Mn_3O_4 and the second to the reduction of CoO. One can thus conclude that the high MnO loading has a positive effect on the reducibility of cobalt: a downward shift of ~20 °C is observed for the reduction to metallic cobalt. This confirms that the in-situ reduction is sufficient for the production of the active phase.

4.2   Catalytic testing

As mentioned previously, the co-precipitated samples were used for 2 purposes: finding reaction optima for Fischer-Tropsch to lower olefin reactions and to function as a reference system for the model catalyst. Initial catalytic tests to establish activity and selectivity were performed at low pressure. In order to find reaction optima -in terms of temperature and pressure-, the FTO reaction conditions were varied. The search for reaction optima is performed utilising high pressure testing (Flowrence), as it easily varies between conditions within 1 catalytic run.

4.2.1   Low pressure testing
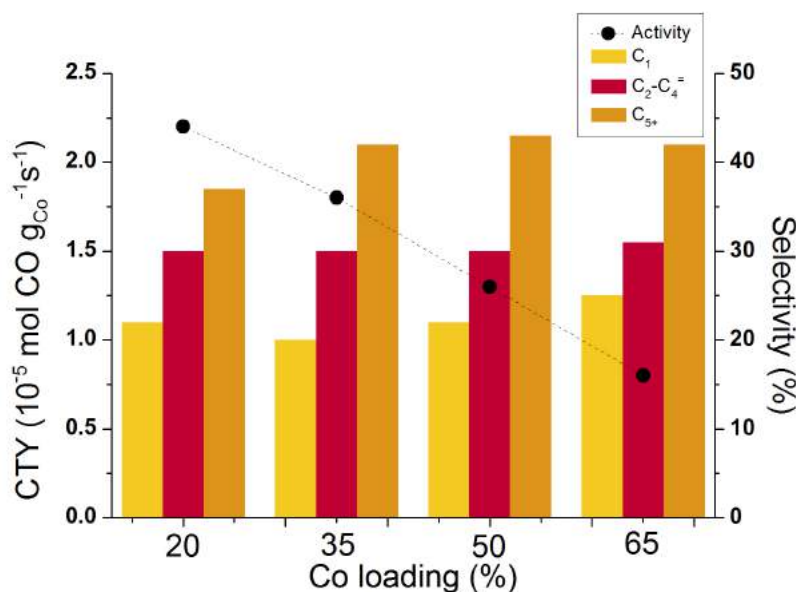
Figure 4.4: Low pressure catalytic performance of the co-precipitated catalysts with varying Co loading. (1 bar, 240 °C, GHSV=4000h^{-1}, H$_2$:CO=2, TOS=23 h)

In the low pressure tests, the catalytic performance (in terms of activity) of the multiple catalysts is remarkably similar, e.g. the lower olefin selectivity is practically identical for all samples. The main differences, if one can name them as such, are the changes in methane and C$_{5+}$ selectivity, yet these seem to fall in the margin of experimental error. Correspondingly, the alpha values are very similar: 0.79, 0.84, 0.83 and 0.82 for Cat 20/80, 35/65, 50/50 and 65/35, respectively.

More interesting is the measured activity of the various samples, it decreases with an increase in Co loading, i.e. an increased MnO loading has a positive effect on the activity. This effect is not found in literature. Typically literature shows the passing through a maximum (at low loadings) in activity with increasing Mn loading.[60, 56]

4.2.2 High pressure testing (Flowrence)

In this section, only the selectivity towards the lower olefin fraction will be presented as this measurement was focussed on optimising the reaction conditions for this product fraction. (The full selectivity for all of the catalysts can be found in the Appendix.) Together with data on the selectivity of the catalysts, information is provided on the activity and the olefin to paraffin (O/P) ratio of C_2-C_4 hydrocarbon chains.
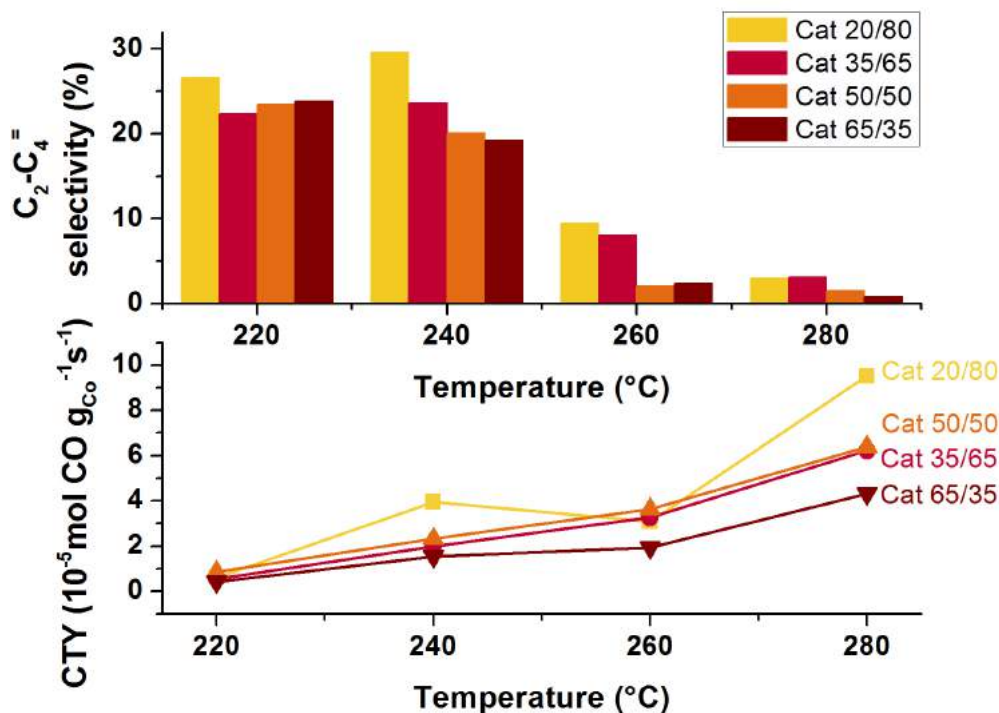
Effect of temperature

Figure 4.5: Temperature dependence of the lower olefin selectivity and activity of the co-precipitated catalysts with varying Co loading. 10 bar, GHSV=2500h^{-1}, H_2:CO=2, TOS=15 h.

Figure 4.5 shows the selectivity and CTY (TOS=15 h) per sample at different temperatures and with a constant pressure of 10 bar. The data clearly shows the detrimental effect on the lower olefin selectivity when raising temperature to high values: it is nearly diminished. Interestingly, the selectivity values for 220 and 240 °C are relatively close together in comparison to the large drop when increasing the temperature from 240 to 260 °C.
These observations are reflected in the calculated alpha values as seen in Table 4.2.

Additionally, a change in temperature can induce a significant change in activity of up to an order of magnitude. By combining the activity and selectivity data, one can conclude that the optimum value for the lower olefin production is 240 °C (at 10 bar), as this combines a reasonably high activity and the best alpha value (close to α=0.5) of the various catalysts . Overall, the best performing catalyst is Cat 20/80, which also happens to show its highest selectivity at 240 °C.

31

Table 4.2: Alpha values calculated from temperature varied Flowrence data. (p=10 bar, GHSV=2500h^{-1}, TOS=15 h, H$_2$:CO=2)

Calculated alpha values				
Sample ID	220 °C	240 °C	260 °C	280 °C
Cat 20/80	0.41	0.59	0.26	0.97
Cat 35/65	0.86	0.54	0.37	0.64
Cat 50/50	0.31	0.61	0.43	0.70
Cat 65/35	0.36	0.53	0.36	0.57

Olefin/paraffin ratio Table 4.3 shows the O/P ratios of the catalysts at varied temperatures.

Table 4.3: Temperature dependence of the O/P ratio of co-precipitated catalysts. (p=10 bar, GHSV=2500h^{-1}, TOS=15 h, H$_2$:CO=2)

O/P ratio				
Sample ID	220 °C	240 °C	260 °C	280 °C
Cat 20/80	3.12	**2.15**	0.60	0.24
Cat 35/65	1.53	1.37	0.31	0.13
Cat 50/50	1.87	1.14	0.07	0.07
Cat 65/35	1.66	1.00	0.15	0.06

This table displays a deterioration in the O/P ratio with an enlarged temperature, implying a preference for the use of a relatively low temperature as a large O/P is desired. The table shows resemblance to the selectivity data in Figure 4.5 when considering the trend in values when augmenting the temperature: the values at 220 °C and 240 °C are comparable and followed by a big drop when moving to 260 °C and 280 °C.

Literature confirms the negative effect of increasing temperature on the O/P ratio.[67, 68] Thermodynamics predict an increase in O/P ratio with temperature, however, kinetics prevent this effect. With increasing temperature, the synthesis of paraffins becomes kinetically more favourable, as with temperature the hydrogenation rate increases as well as the desorption rate, resulting in a lowering of the alpha value.[69, 70]

Pressure dependence

Analogous to the temperature, the pressure dependence was evaluated, i.e. the temperature was kept constant at 240 °C while the pressure was varied (5, 10, 15 and 20 bar). The activity and selectivity data is given in Figure 4.6
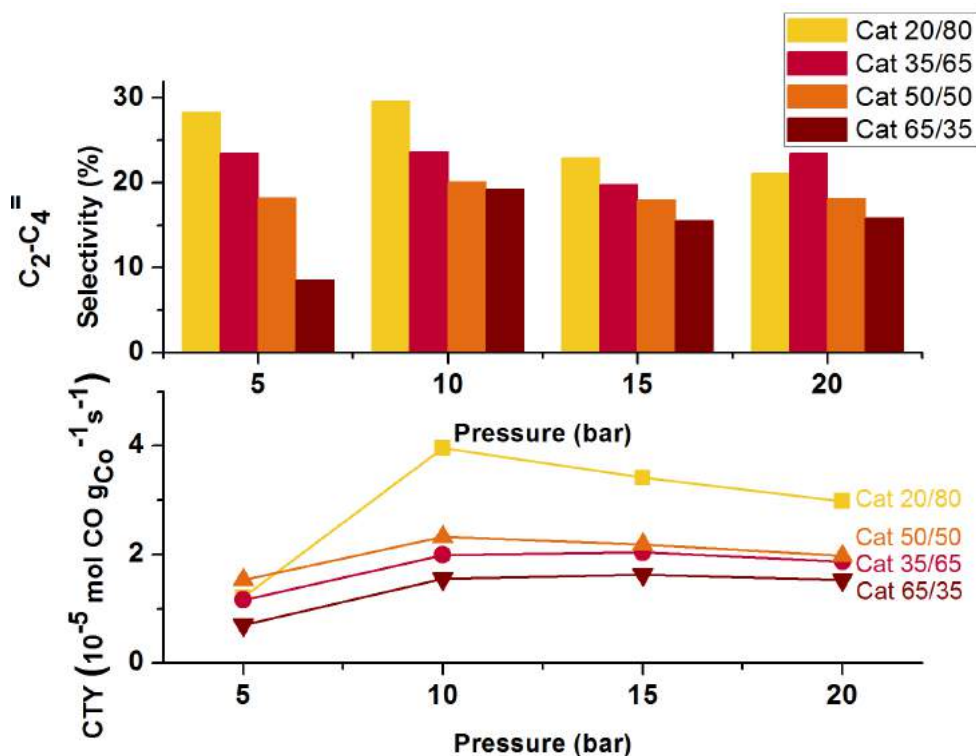
Figure 4.6: Pressure dependence of the lower olefin selectivity and activity of the co-precipitated catalysts with varying Co loading. 240 °C, GHSV=2500h^{-1}, H$_2$:CO=2, TOS=15 h.

The pressure has a slighter, yet still significant, effect on the selectivity of the catalysts than the temperature. The general trend in the presented data is that a peak in selectivity and activity is acquired, i.e. the optimum pressure. For the selectivity, an optimum is found at 10 bar. For the activity the peak is not immediately obvious for all catalysts, the activity values at 10 and 15 bar often vary little. Additionally, the alpha values vary little, as can be seen in Table 4.4.

Table 4.4: Alpha values calculated from pressure varied Flowrence data. (240 °C, GHSV=2500h^{-1}, TOS=15 h, H$_2$:CO=2)

Calculated alpha values				
Sample ID	5 bar	10 bar	15 bar	20 bar
Cat 20/80	0.59	0.59	0.45	0.40
Cat 35/65	0.46	0.54	0.57	0.41
Cat 50/50	0.34	0.61	0.55	0.50
Cat 65/35	0.46	0.53	0.50	0.42

The selectivity data, for both the temperature and pressure dependent tests, indicate that Cat 20/80 is the best performing catalyst and can therefore be elected as reference catalyst. When one looks at the temperature and pressure dependence of this sample, one can construct the correlation graphs seen in Figure 4.7.
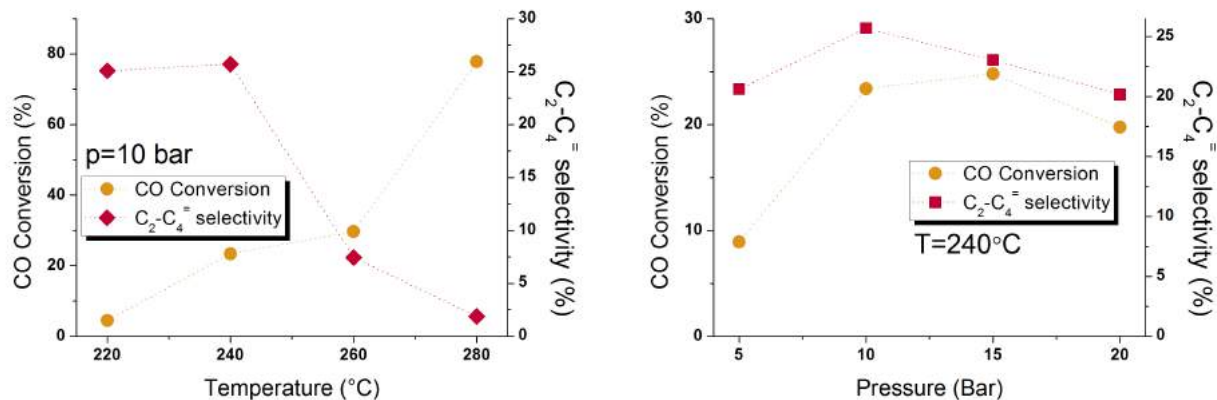
Figure 4.7: Plots showing the correlation between the activity and selectivity with **left:** temperature and **right:** pressure.

Using the lower olefin selectivity as deciding factor for condition optima, the optima are determined to be $240\,°C$ and 10 bar pressure.

Olefin/paraffin ratio

The trend over the spectrum of pressures is again a peak in the O/P ratios. The catalysts, with exception of Cat 50/50, show this peak value at 10 bar. Cat 50/50 is the only sample to show a structural increase of the O/P ratio upon pressure increase. However, the O/P ratio values for 10 and 15 bar lie extremely close together, so -with reserve- one can assume that the overall optimal pressure for the O/P ratio, is at 10 bar.

Table 4.5: Pressure dependence of the O/P ratio of co-precipitated catalysts. ($240\,°C$, GHSV=2500h^{-1}, TOS=15 h, H$_2$:CO=2)

	O/P ratio			
Sample ID	**5 bar**	**10 bar**	**15 bar**	**20 bar**
Cat 20/80	1.42	2.15	1.51	1.35
Cat 35/65	1.36	1.37	1.16	1.11
Cat 50/50	0.70	1.14	1.15	1.23
Cat 65/35	0.29	1.00	0.82	0.89

5

Model catalyst

5.1 Characterisation

5.1.1 TEM

Using TEM, the shape and size of synthesised colloidal particles, and their homogeneity, could be determined. Additionally, the effects of various synthesis parameters, as well as synthesis reproducibility, could be visualised.

A typical synthesis (parameter set 1), as described in the experimental section, would yield particles such as depicted in Figure 5.1.
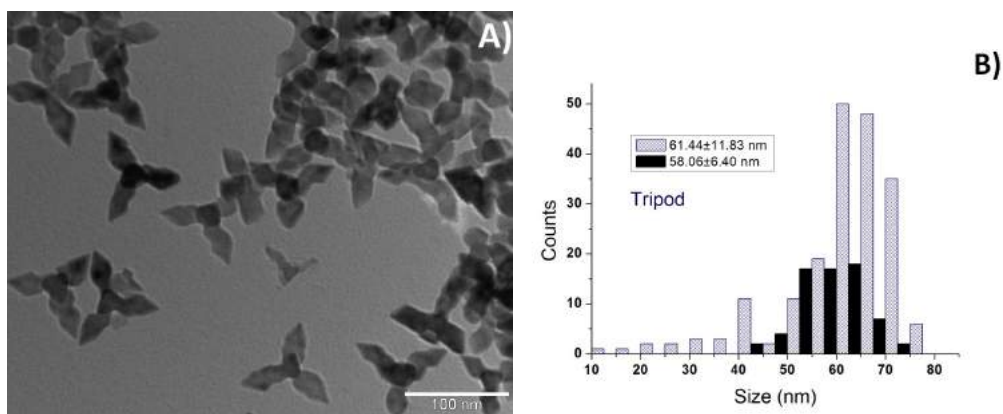

Figure 5.1: **A:** TEM image of colloidal particles yielded by a typical colloidal synthesis and **B:** the particle size distribution of two colloidal samples.

These particles can seemingly be divided in two parts: the core and the "wings", which add up to particles of approximately 60 nm. One can readily see that the shown sample was not fully homogeneous, for example when one compares the particles in the bottom left and top right corner. This initial synthesis result was used to describe the effects of synthesis parameters, as well as its reproducibility.

Reproducibility

A characteristic of colloidal synthesis is that it can exercise a large amount of control over resulting particles by carefully screening various parameters, such as the temperature, the heating rate, the degree of vacuum used etc. However, this makes the synthesis vulnerable to a large amount of experimental errors: little differences in the synthesis, e.g. the temperature at which vacuum is applied or the flow speed of the N_2-gas, can yield a radically different result. Figure 5.2 shows four images of four seemingly identical syntheses.
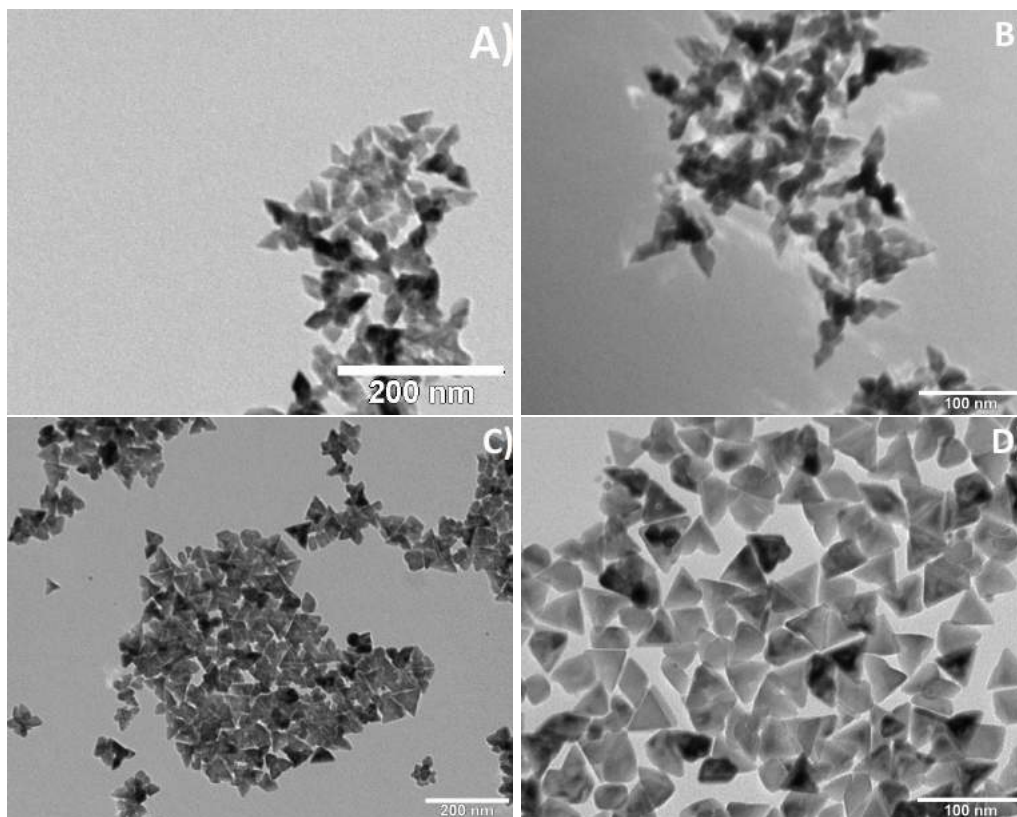
Figure 5.2: **A-D:** TEM images showing examples of poor reproducibility in a typical colloidal synthesis.

Figure 5.2 A-D exemplifies the troublesome reproducibility. For example, samples C-D were produced using a seemingly identical synthesis procedure, but with a different supply of $Mn_2(CO)_{10}$. Other factors that were of influence on the reproducibility were, for example, the flask size (50-100 mL), stirring rate, degassing time, the hot injection (temperature, air in the precursor solution, number of injections needed for hot injection), N_2-flow speed, degree of vacuum, etc. Through repetition and practise, the synthesis was made fully analogous, thereby yielding reproducible colloidal particle syntheses, the results of which are shown in Figure 5.3.
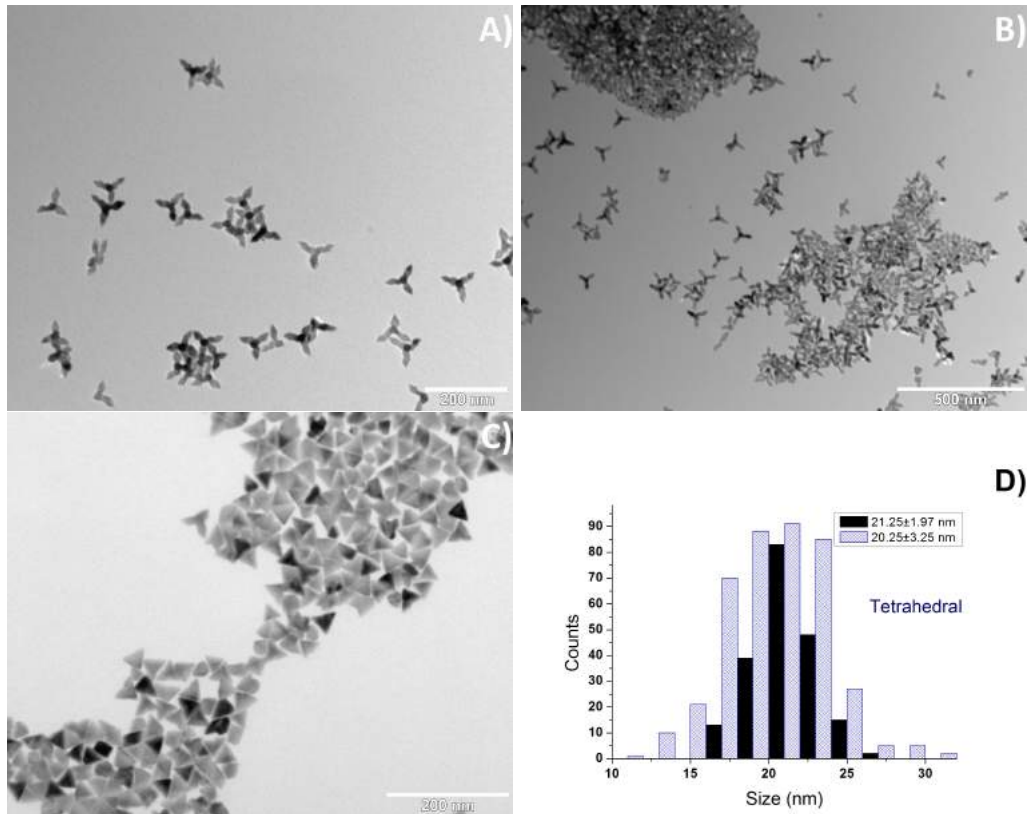
Figure 5.3: **A-C:**TEM images of colloidal particles with good reproducibility, **D:** the particle size distribution of 2 tetrahedral samples with an average size of approximately 20 nm.

Subsequently, the effect of synthesis parameter variation was studied. Some examples of parameter variation effects are given below.

Effect of scaling

The reaction volume is of influence on the resulting particles. As an effect of the increase in amounts of all reactants used (x2), the tripod particles became more corrugated and the tetrahedral particles lost their homogeneity, as is depicted in Figure 5.4.
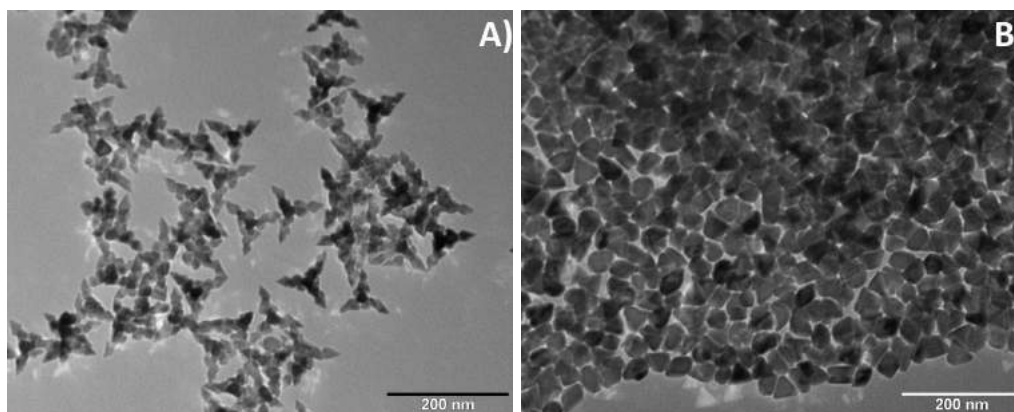
Figure 5.4: **A-B:** TEM images of colloidal particles produced using a scaled up synthesis.

Effect of heating rate

The effect of the heating rate during the heating from the hot injection temperature to the nucleation temperature is of influence on the particle shape and sample homogeneity, as is depicted in Figure 5.5. Both the tripod particles and the tetrahedral particles lose their well defined shapes when utilising a lower heating rate.
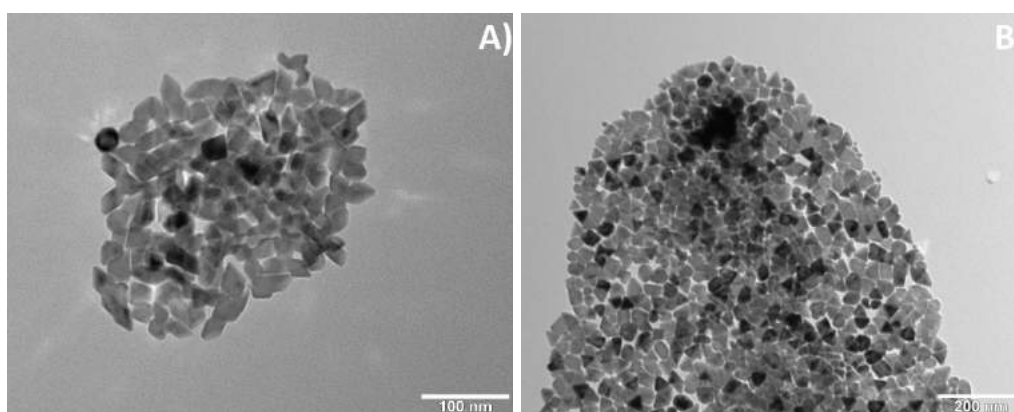

Figure 5.5: **A-B:** TEM images of samples synthesised with a lower heating rate with a loss in particle shape uniformity as a result.

Effect of structure directing agent

The effect of the amount of structure directing agent (oleylamine) in the reaction mixture is visible in Figure 5.6. In the absence of structure directing agent, the tetrahedral particles lost their characteristic shape and aggregated, while an excess (1 mmol, see Table 3.3) caused the particles to become very well defined tetrahedrals.
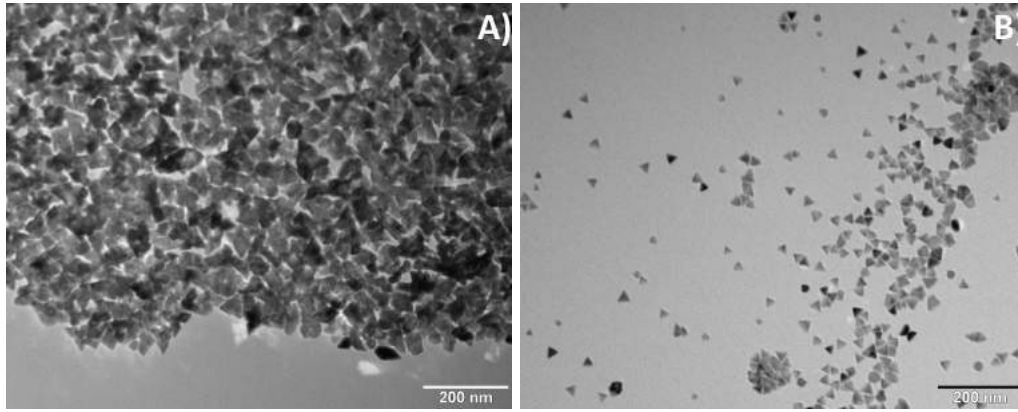
Figure 5.6: TEM images of particles synthesised using **A:** no, or **B:** an excess of structure directing agent.

Effect of Co:Mn ratio

The use of an increased amount of metal precursor solvent (see Experimental procedure) resulted in an increased amount of dissolved manganese precursor and an increased manganese loading in the resulting particles (76 at%, ICP, see Appendix). The effect of the Co:Mn ratio becomes evident in Figure 5.7. In the absence of $Mn_2(CO)_{10}$, large agglomerates were formed. However, separate hexagonal colloids of approximately 20 nm formed when using an increased amount of $Mn_2(CO)_{10}$. The Co:Mn thus has a significant effect on the resulting particle shape.
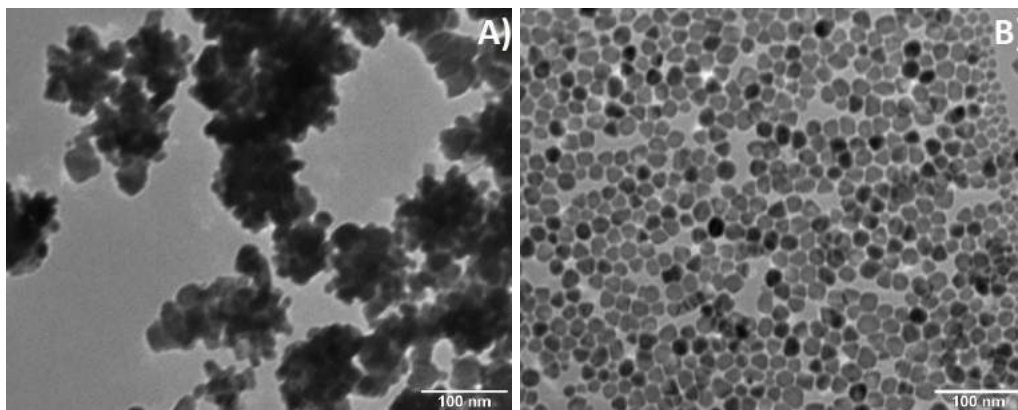

Figure 5.7: TEM images of **A:** pure cobalt colloids, and **B:** colloids with an increased Mn loading.

Effect of injection temperature

The effect of the hot injection temperature becomes evident in Figure 5.8. An increased injection temperature (140 °C rather than 90 °C) lead to a drop in average particle size from 20 nm to 16 nm.
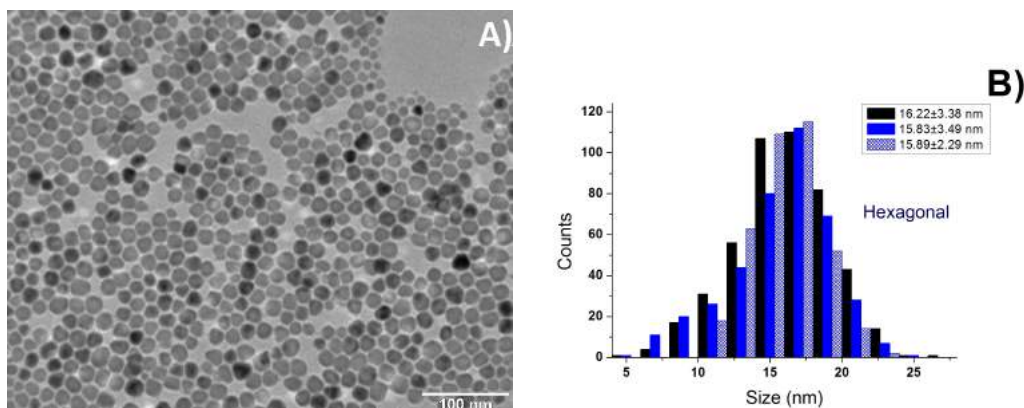
Figure 5.8: TEM image of **A:** Hexagonal particles synthesised with an increased hot injection temperature (140 °C) with an accompanying particle size distribution of 3 samples of hexagonal particles (**B**).

Effect of calcination

The effect of post-synthesis calcination (400 °C, 2 hours, flowing air) is visible in Figure 5.9. The images show the seemingly unchanged tetrahedral particle shape and the slightly increased size (25 nm). The aggregation of the particles may be due to the release of the stabilising surfactants present on the surface during the calcination, thereby decreasing the inter-particle electronic repulsion.
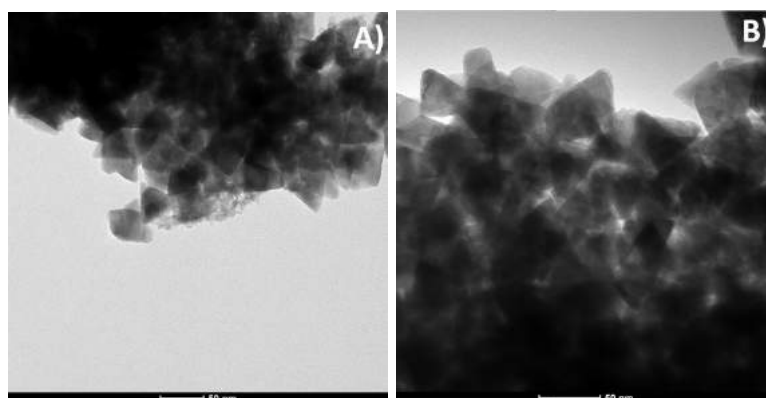

Figure 5.9: **A-B:** TEM images of calcined tetrahedral particles.

Deposition on CNT

The deposition of tripod particles on CNTs was also characterised using TEM. Figure 5.10 shows the attachment of a few colloids. Due to the low level of attachment (determined with TGA-MS, see Appendix) it was difficult to effectively characterise the system using TEM, apart from the assessment that the deposition of the colloidal particles was not very successful.
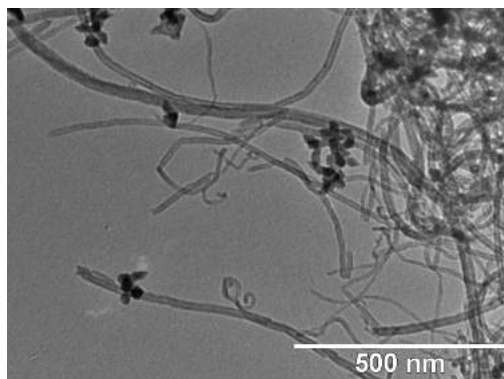
Figure 5.10: Tripod colloidal particles attached to CNTs.

5.1.2   STEM-EDX

The elemental analysis of the tetrahedral and hexagonal particles showing the distribution of both elements is given in Figure 5.11.
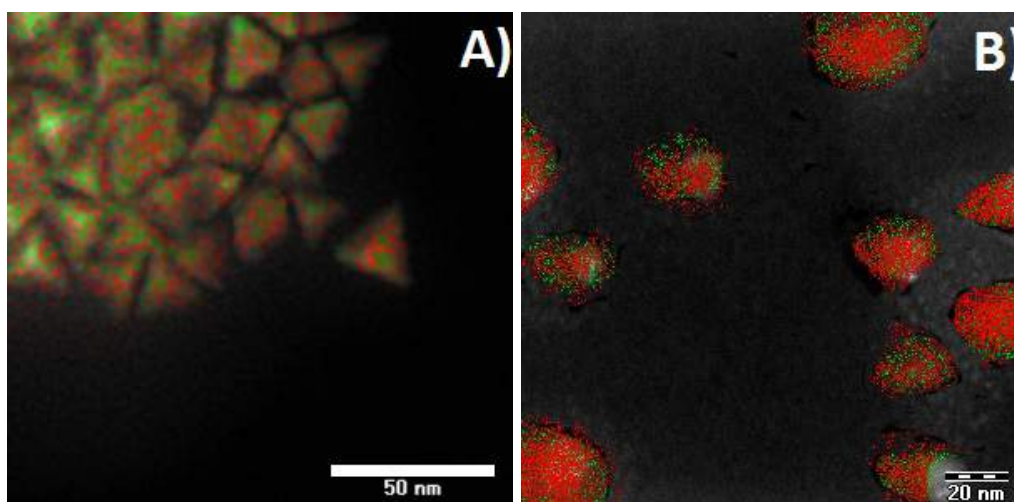

Figure 5.11: The elemental distribution of cobalt (green) and manganese (red) in **A:** tetrahedral and **B:** hexagonal colloidal particles.

From the images it becomes clear that the hexagonals are richer in Mn (red) content compared to the tetrahedrals. Additionally, the images show a homogeneous distribution of cobalt and manganese throughout both types of particles. TEM and STEM-EDX have thus shown the potential of colloidal synthesis to reproducibly produce monodisperse (in size and shape) particles with a uniform distribution of elements.

5.1.3   XRD

The bulk crystal structure of fresh and calcined colloidal particles (tetrahedral and hexagonal) was probed using XRD. Figure 5.12 shows the diffractograms of both the fresh catalysts. Fits show that both samples are comprised of separate CoO and MnO phases (CoO mostly visible as peak broadening), however different

peak intensities give varying Co:Mn compositions. The broad signal at $2\theta=10°$ is due to the SiO_2 diluent of the samples. Table 5.1 summarises the XRD data. It should be noted that for the non-calcined tetrahedral particles, the fit was incomplete, i.e. the fit did not fully explain al features of the diffractogram. As a result, the calculated Co:Mn ratio may deviate from the actual value.
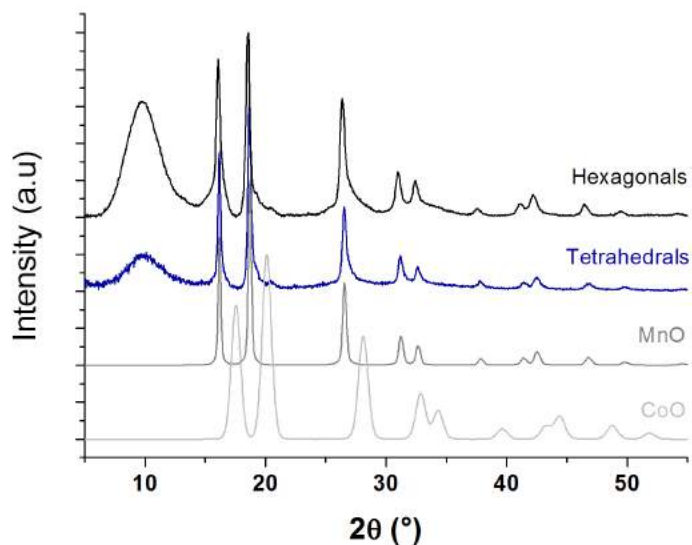

Figure 5.12: XRD diffractograms of hexagonal (black) and tetrahedral colloidal particles (blue), with CoO and MnO fits.

Figures 5.13 **A**&**B** show the effect of calcination (400 °C, 2 hours) on the bulk crystal structure of the colloidal particles. Fitted structures show that the particles now consist of mixed Co/Mn spinel structures (similar to the reference catalyst), resulting in an increased oxidation state for both Co and Mn from 2+ to 3+. Additionally, fitting revealed that the crystallinity increases upon calcination: the strain within the crystal structure is relaxed in comparison to the fresh samples. An overview of the data obtained using XRD is given in Table 5.1.
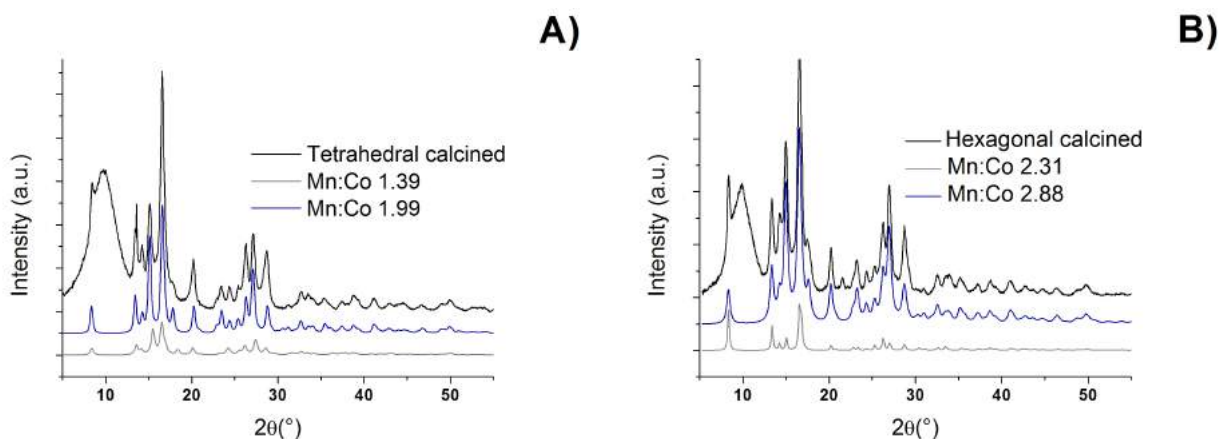
Figure 5.13: XRD diffractograms of calcined tetrahedral (**A**) and hexagonal colloids (**B**) including fits calculated by Rietveld analysis.

Table 5.1: Summary of XRD data on the fresh and calcined colloidal particles.

Catalyst ID	Treatment	Used fit	Species crystallite size(nm)	Co:Mn
Tetrahedral	-non-calcined	CoO	6	27:73
		MnO	13	
	-calcined	Spinel Mn:Co 1.39	10	42:58
		Spinel Mn:Co 1.99	17	
Hexagonal	-non-calcined	CoO	4	30:70
		MnO	13	
	-calcined	Spinel Mn:Co 2.31	25	26:74
		Spinel Mn:Co 2.88	10	

5.1.4 XPS

To verify the uniformity of the bulk and surface structure, the surfaces of the fresh and calcined colloids were analysed with XPS. The Co_{2p} spectra are given in Figure 5.14. The oxidation state is given by the $Co_{2p_{3/2}}$ peak position in combination with the intensity of satellite features. For the calcined tetrahedral species, a lack in intensity could be due to a low presence of cobalt on the surface of these particles. This lack in intensity could be due to manganese species migration towards the surface during calcination.

The relevant data from these two figures is summarised in Table 5.2. One can thus see that both the fresh samples present XPS peaks at the same values. Therefore, it can be asserted that both samples contain a similar surface in terms of structure.
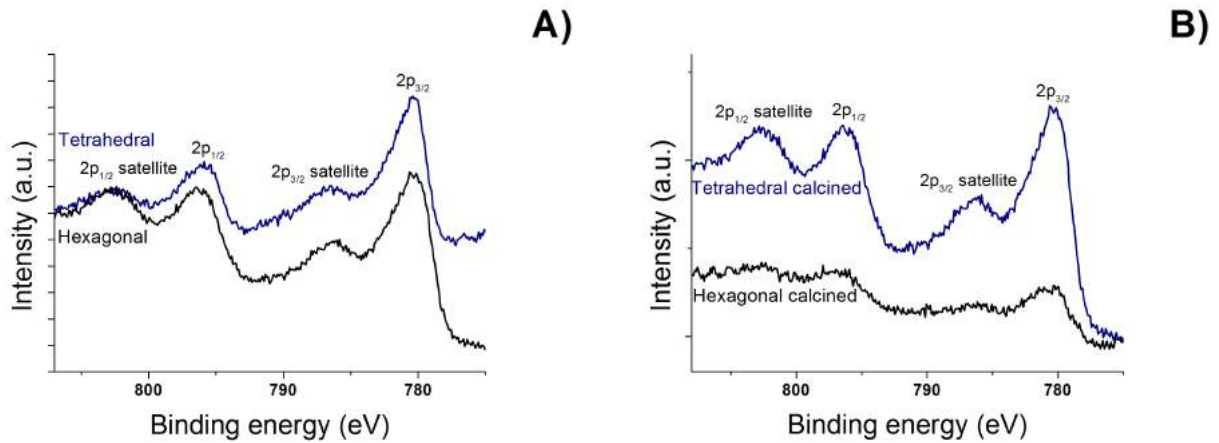
Figure 5.14: Co_{2p} XPS spectra for **A:** the fresh and **B:** the calcined colloidal catalysts.

Table 5.2: Summary of Co_{2p} XPS data.

Treatment	Catalyst ID	$Co_{2p}^{3/2}$	$Co_{2p}^{1/2}$	$Co_{2p}^{3/2}$ satellite	$Co_{2p}^{3/2}$ satellite	Co oxidation state
Fresh	Tetrahedral	780.6	786.3	796.9	803.0	2+
	Hexagonal	780.4	786.5	795.9	802.4	2+
Calcined	Tetrahedral	780.4	785.1	786.3	795.7	3+
	Hexagonal	n.a.	n.a.	n.a.	n.a.	n.a.

The Mn_{3s} spectra are depicted in Figure 5.15. Using the Mn_{3s} peak splitting (i.e. ΔE), the oxidation states for the Mn species were determined. In the spectra, the difference in tetrahedral and hexagonal colloids is visualised: the Mn_{3s} intensity is higher for the tetrahedral particles, indicating a higher Mn content for the tetrahedrals. Calcination results in an enhanced intensity difference. Together with the Co_{2p} XPS data, the spectra seem to indicate Mn migration to the surface of the hexagonal particles during calcination. The relevant Mn_{3s} XPS data is summarised in Table 5.3.
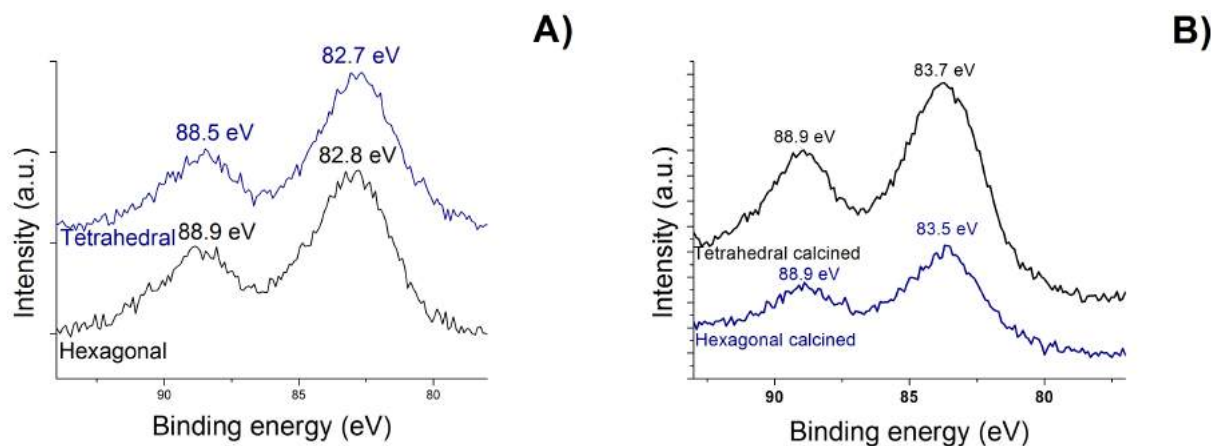
Figure 5.15: Mn$_{3s}$ XPS spectra of **A:** the fresh and **B:** the calcined colloidal particles. The peak positions are indicated within the Figures.

Table 5.3: Summary of Mn$_{3s}$ XPS data.

Treatment	Catalyst ID	Peak 1 (eV)	Peak 2 (eV)	Peak separation (eV)	Mn oxidation state
Fresh	Tetrahedral	82,85	88,62	5,77	2+
	Hexagonal	83,08	88,76	5,68	2+
Calcined	Tetrahedral	83,59	88,78	5,19	3+
	Hexagonal	83,68	88,95	5,27	3+

As Table 5.3 shows, calcination results in a change in oxidation state from 2+ to 3+, corresponding to a change from the separate metal mono-oxides to a (mixed) spinel structure. The XPS and XRD analyses show the uniformity of the colloidal particles in terms of bulk and surface structure.

From the XPS data the Co:Mn ratio of the catalyst surfaces was calculated, the results are shown in Table 5.4.

The table shows that, even though a structural reformation occurs, no species migrate to or from the surface of the tetrahedral particles: the distribution seems to remain uniform. The suspected migration of Mn species to the surface of the hexagonal particles can be explained by the higher Mn loading of these particles.

Table 5.4: Co:Mn ratios calculated from the relative XPS Co:Mn peak intensities.

Catalyst ID	Treatment	Co:Mn
Tetrahedral	Fresh	46:54
	Calcined	46:54
Hexagonal	Fresh	16:84
	Calcined	n.a.

5.2   Catalytic testing

5.2.1   Low pressure testing

The low pressure catalytic data for the tetrahedral and hexagonal particles is given in Figure 5.16. Although both the tetrahedral and hexagonal colloidal particles consist of the same crystal structure (a mix of separate CoO and MnO, see XRD), significant differences were encountered during FTO testing.
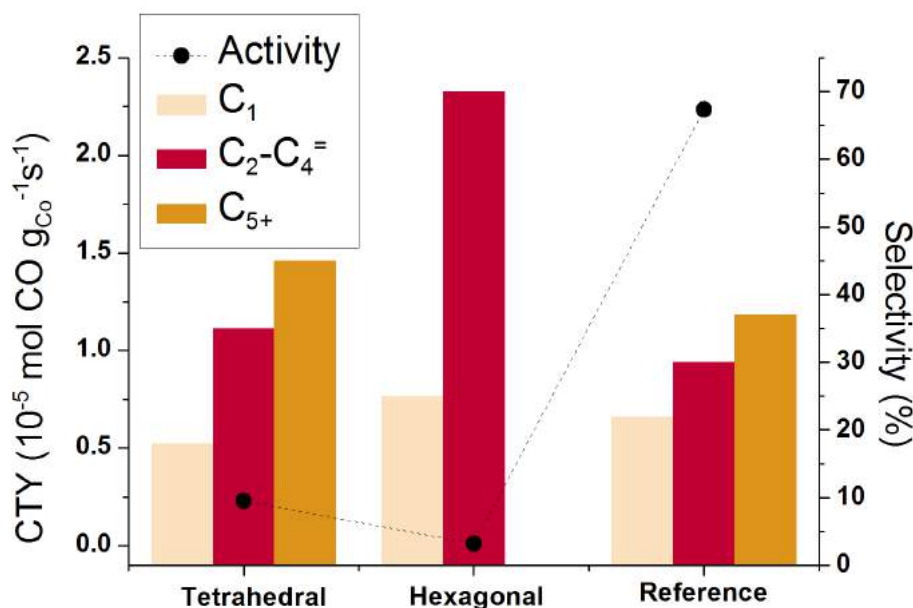

Figure 5.16: Low pressure catalytic performance (activity and selectivity) of colloidal particles together with reference catalyst (Cat 20/80) data. 240 °C, 1 bar, GHSV=4000h^{-1}, H$_2$:CO=2, TOS=23 h.

In the figure the effect of the use of different colloidal particle types is visualised: a decrease in activity upon moving from tetrahedral → hexagonal particles. The main difference between these particles is their Co:MnO ratio, therefore, it is suspected that the increased MnO loading induces this drop in activity. Possibly it influences the reducibility of cobalt, i.e. the cobalt oxide has not fully been reduced to the active phase during the reduction treatment, thereby reducing the activity. However, TPR measurements of the reference catalyst showed a positive effect of MnO on the reducibility of Co ((inconclusive)TPR measurements of the colloidal catalyst are shown in the Appendix). Another reason might be that the MnO (partially) covers the cobalt surface, effectively shielding the cobalt surface from incoming reactants. XPS did show a possible migration of Mn species during calcination, i.e. a heat treatment. Therefore, it may be that the reduction and/or catalytic testing induce a migration of Mn to the surface, thereby lowering the activity.

Another possible effect of the increased MnO loading is the immense shift towards the lower olefin fraction for the hexagonal particles (also reflected in the alpha value, see Table 5.5), however one needs to be cautious with these results. In the obtained gas chromatograms a challenge immediately presented itself: for the hexagonal particles, it was hard to distinguish between peak and noise, effectively quenching the quantifiable C$_{5+}$

selectivity. Therefore, as these results were acquired with too little CO conversion, resulting in the scattering of the data, the accompanying selectivity is scarcely reliable.

Table 5.5: Selectivity of tetrahedral and hexagonal colloidal particles under standard testing conditions. $240\,^{\circ}$C, 1 bar, GHSV=4000h^{-1}, H$_2$:CO=2, TOS=23 h

Catalyst	O/P	α
Tetrahedral	17.5	0.86
Hexagonal	14	0.54
Reference	6	0.79

If one compares the tetrahedral catalyst with the reference catalyst, it appears that the tetrahedral catalyst outperforms the reference catalyst in terms of selectivity: the methane fraction is lower and the useful lower olefin and C$_{5+}$ fractions are increased with respect to the reference catalyst. However, the lower olefin fractions are not the main fraction of these catalysts, thus categorising them a FTS rather than a FTO catalyst. This is reflected in the alpha values: 0,86 and 0,79 for the tetrahedral and reference catalyst, respectively.

By decreasing the syngas flow, and by increasing the catalyst loading in the reactor, it was tried to increase the CO conversion of a catalyst. By increasing the CO conversion of the hexagonal colloids, the effect of an increased MnO loading could be studied with more trustworthiness (less scattering of data). The resulting catalytic data is shown in Figure 5.17.

The undertaken measures did increase the CO conversion (an increase from 0,03 to 0,05 % CO conversion min^{-1} for the low flow measurement), yet a larger increase in CO conversion was expected: the amount of used catalyst was approximately triple the amount used in the original measurement (50 mg rather than 18 mg). This in combination with a decreased syngas flow would lead to an expectation of at least double the CO conversion, compared to the standard FTO test. However, a significant decrease in the signal-to-noise ratio was observed in the gas chromatograms, thus giving more credibility to the measured selectivity. The selectivity is mainly towards the C$_2$-C$_4$$^=$ fraction, the C$_{5+}$ fraction is very small, however, there is quite a large production of methane.

Table 5.6: O/P ratios and alpha values for multiple catalytic tests. $240\,^{\circ}$C, 1 bar, H$_2$:CO=2, TOS=23 h. Standard: GHSV=4000h^{-1}, low flow: GHSV=1100h^{-1}

Sample	O/P	α
Hexagonal low flow	14	0.47
Hexagonal	14	0.54
Tetrahedral	17.5	0.86

When comparing the low flow measurement of the hexagonal particles to the standard measurement of the tetrahedral particles, significant differences in both activity and the selectivity were observed. Whereas the tetrahedral colloidal particles seem to behave as a FTS catalyst, the hexagonal catalyst interestingly behaves as a FTO "catalyst", which is seen in the alpha values in Table ?? (0,86 and 0,47 for the tetrahedral and hexagonal, respectively). Therefore it is assumed that indirectly the Co:Mn ratio is of tremendous
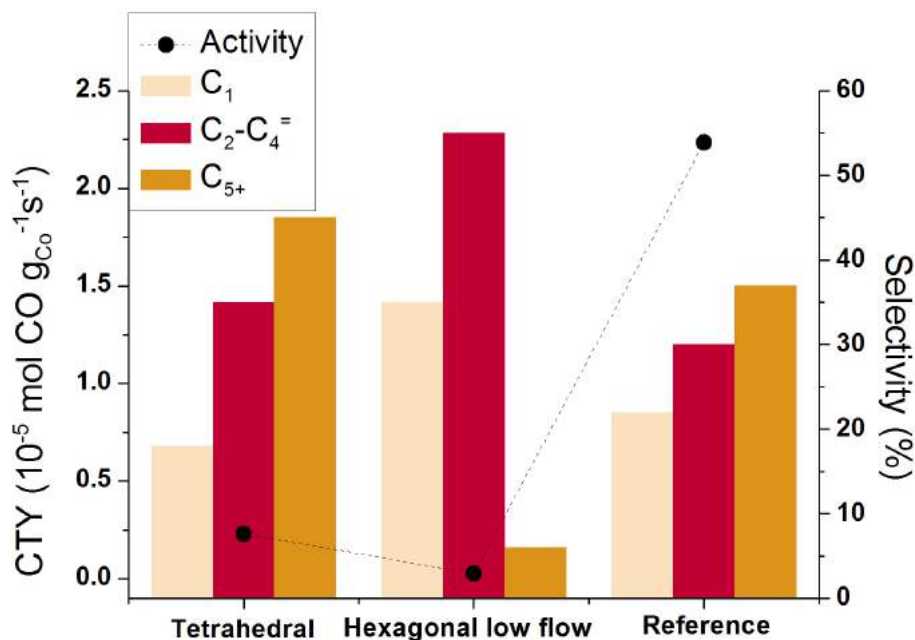
Figure 5.17: Low pressure catalytic performance (activity and selectivity) of the colloidal particles together with reference catalyst data, with decreased syngas flow and increased catalyst loading for the hexagonal particles (H_2:CO=4:2 mLmin^{-1}, 50 mg of hexagonal catalyst, GHSV=1100h^{-1}). 240 °C, 1 bar, GHSV=4000h^{-1}, H_2:CO=2, TOS=23 h.

importance in CoMnO catalyst synthesis: by varying the Co:Mn ratio, the properties of the colloids are influenced (e.g. shape, surface composition, particle size), resulting in altered catalytic performance. However, the O/P ratios are comparable for both catalysts (yet both were high in comparison to the reference catalyst).

Reduction in CO

To investigate whether the use of CO gas during the in-situ reduction has a positive effect on the lower olefin selectivity, an in-situ reduction step in CO flow rather than in H_2 flow was used for the tetrahedral and the reference catalyst.[71, 72] As Table 5.7 shows, the intended results were not obtained.

Table 5.7: Activity and selectivity of the tetrahedral and reference catalyst after reduction in CO. 240 °C, 1 bar, GHSV=4000h^{-1}, H_2:CO=2, TOS=23 h.

CTY(10^{-5} mol CO $g_{Co}^{-1}s^{-1}$)		Selectivity (%)			
Sample	CTY	C_1(%)	C_2-$C_4$$^=$(%)	C_{5+}(%)	O/P
Tetrahedral	0.01	55	30	10	6
Reference	0.3	25	30	40	6

For the reference catalyst the activity was approximately halved. The tetrahedral catalyst its CO con-

48

version was lowered with a factor of 15. Inspection of the selectivity reveals that for the reference catalyst, the reduction in CO has little to no effect. For the colloidal catalyst, reduction in CO has a negative effect: more than half of the product stream consists of methane. A possible explanation for these effects may be that a reduction treatment in CO is unable to fully convert the present cobalt oxide to cobalt metal, thereby reducing the activity per gram of cobalt.

5.2.2   FTO testing of calcined colloidal CoMnO

A sample of calcined tetrahedral particles was used for low pressure testing. Figure 5.18 depicts the activity and selectivity of the calcined catalyst compared to the fresh tetrahedral catalyst and reference catalyst.
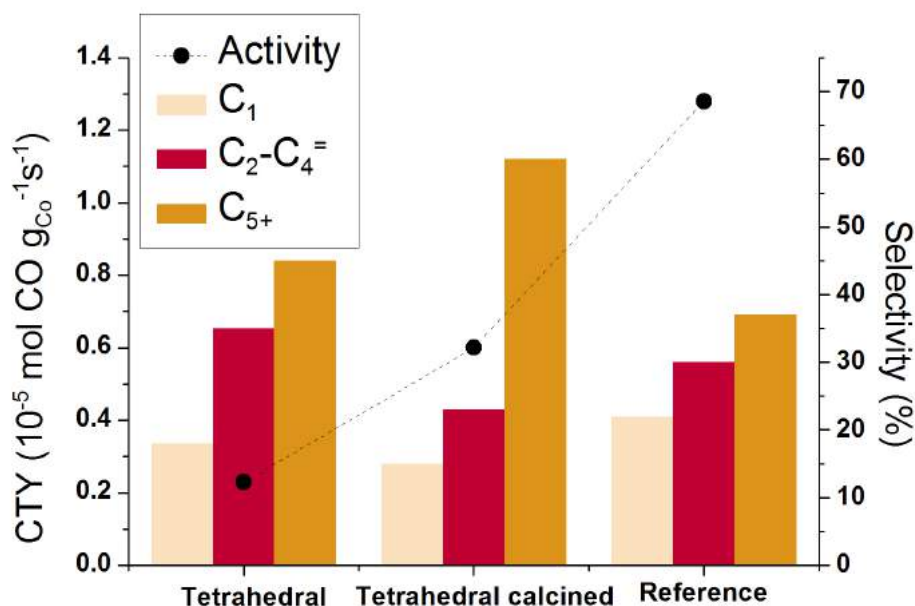

Figure 5.18: Low pressure catalytic performance (activity and selectivity) of calcined tetrahedral particles together with fresh tetrahedral and reference catalyst data. Testing of catalysts at 240 °C, 1 bar, $GHSV_{fresh}$=4000h^{-1}, $GHSV_{calcined}$=5800h^{-1} H_2:CO=2, TOS_{fresh}=23 h, $TOS_{calcined}$=11 h.

Figure 5.18 shows the positive effect of calcination on the activity, and the negative effect on the lower olefin selectivity. This indicates that a (mixed) cobalt spinel structure is preferred over a (separate) cobalt mono-oxide for these FT reactions in terms of CO conversion. This could either be a proximity (of Co and Mn species) effect, or a crystal structure effect.

The lower activity compared to the reference catalyst could be explained by the lower MnO loading, as both low and high pressure tests indicated for the co-precipitated catalysts that a decrease in MnO loading resulted in a loss of activity. Additionally, a deviation in active surface species (concentration) may result in this observed lower activity.

Table 5.8: O/P ratios and alpha values for multiple catalytic tests. 240 °C, 1 bar, GHSV$_{fresh}$=4000h^{-1}, GHSV$_{calcined}$=5800h^{-1} H$_2$:CO=2, TOS$_{fresh}$=23 h, TOS$_{calcined}$=11 h.

O/P ratio and alpha value		
Sample	O/P	α
Tetrahedral, calcined	15	0.95
Tetrahedral	17.5	0.86
Reference	5	0.79

Interestingly, the decrease in lower olefin selectivity is accompanied by an increase in C$_{5+}$ selectivity, as is reflected in the alpha value of 0.95 (Table 5.8). It seems that calcination is thus an effective tool to increase the FTS potency of a colloidal CoMnO catalyst. However, this alpha value is remarkably, and unexpectedly high. The alpha value calculations are shown in the Appendix.

High pressure (Flowrence)   The data from the high pressure tests of the tripod colloidal particles and their resulting temperature and pressure optima is given in the Appendix.

5.3   Spent catalyst

With TEM, the spent catalyst were characterised to visualise their thermal stability/structural integrity.

Tetrahedral   Figure 5.19 shows two TEM images of (mostly) tetrahedral particles used for low pressure FTO testing. These images show that the particles remain present as separate colloids, with roughly the same shape and size (an average increase of 20 to 25 nm). Additionally, a remarkable feature is present in Figure 5.19: the formation of carbon filaments.
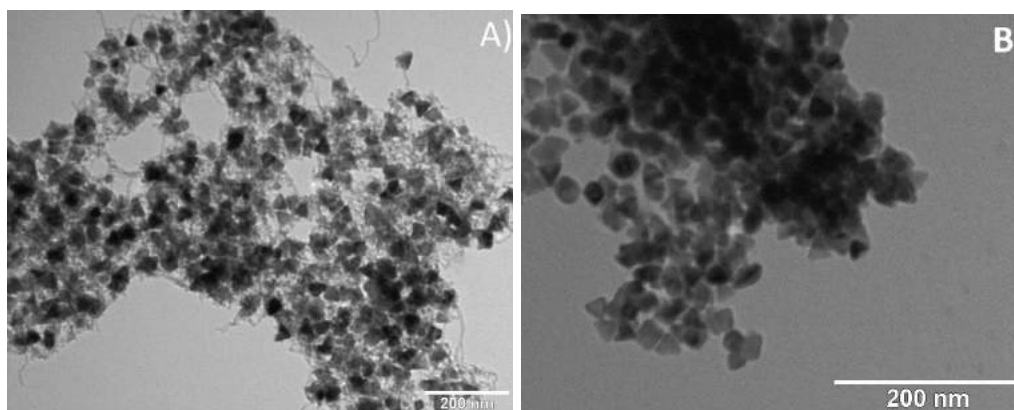

Figure 5.19: **A-B:** TEM images of two samples of spent tetrahedral colloidal particles. 240 °C, 1 bar, GHSV=4000h^{-1}, H$_2$:CO=2, TOS=23 h.

Hexagonal   In the TEM image (Figure 5.20) for the spent hexagonal particles (low pressure testing), it is again seen that the particles have not fully sintered: one can still spot the particle outlines, even though they are aggregated. The size of the particles has increased, but only slightly (16to 20 nm).
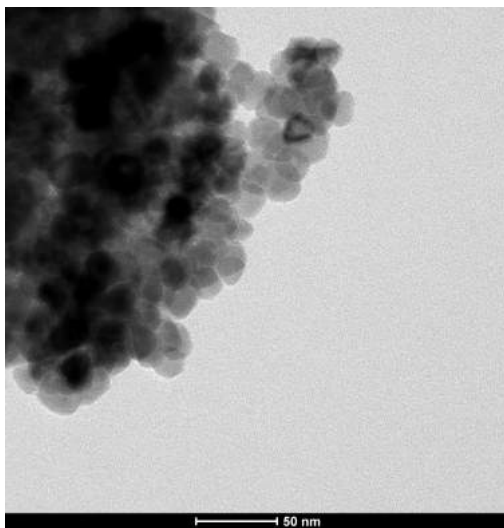

Figure 5.20: TEM image of spent hexagonal colloidal particles. 240 °C, 1 bar, GHSV=4000h^{-1}, H$_2$:CO=2, TOS=23 h.

Calcined tetrahedral   In the TEM images of the spent calcined colloids (Figure 5.21), multiple features were seen. The sample partially remains true to form, i.e. tetrahedral, whereas (a small) part of the sample seems to fully have lost their structural integrity. It is assumed that due to the release of the surfactants, either during the calcination or reduction, the particles cluster, making them more susceptible to sintering and particle growth. As the calcination temperature is higher than the reduction temperature (400 °C compared to 350 °C), this process is more likely to occur during the calcination treatment as was also seen in Figure 5.9.

When Figures 5.9 and 5.21**A** are compared, these images seem to show similar features. From this one can conclude that reduction/catalytic testing does not induce significant sintering. These particles thus must possess substantial thermal stability, even without stabilising surfactants. Additionally, in these spent particles no carbon filaments were found.
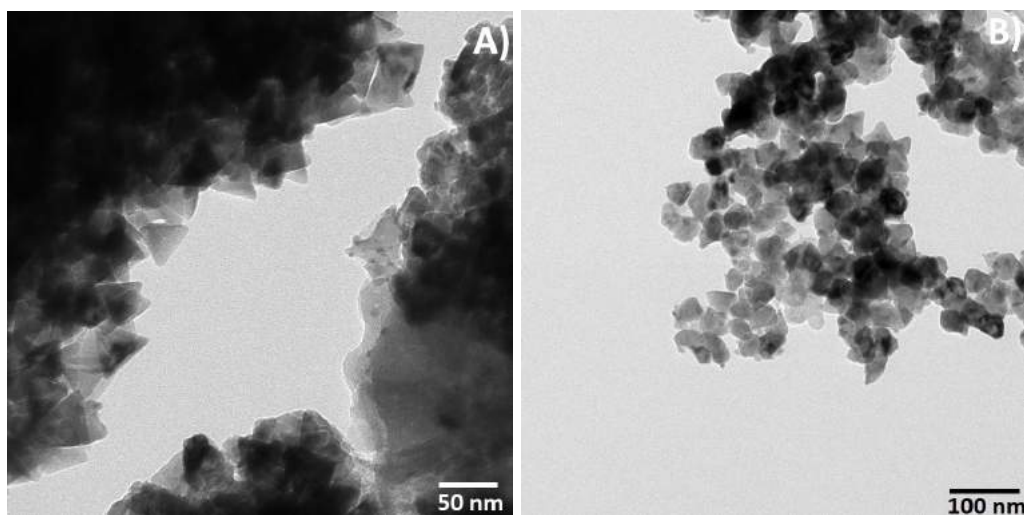
Figure 5.21: **A-B:** TEM images of spent calcined tetrahedral catalyst. 240 °C, 1 bar, H$_2$:CO=2, TOS=24 h

6

Discussion

As interesting as the colloidal systems are on their own, it is relevant to place them within context with results achieved in literature. Therefore, in this chapter first, the comparison between the two types of colloidal particles will shortly be summarised. Second, the colloidal particles will concisely be compared with the reference catalyst. Lastly, the performance of the model catalysts will be collated with catalysts described in the theory section of this work.

6.1   Colloidal particles

A change in reaction parameters within the colloidal synthesis yields different types of colloidal particles. There is potential that by separately changing these parameters, a wide array of colloidal particles can be made, varying in size, shape, composition etc. with as a result a varying potential to selectively convert syngas to lower olefins. It is beyond the reach of this work to give a structural overview of the effect of a change in single/multiple reaction parameters on the FTO performance. However, some remarks can be made about the influence of used parameters, these are given in Table 6.1.

Most of the observed effects are easily explained, they follow colloidal physics. [73] However, some are harder to explain, i.e. the change in product shape upon the variation of the Co:Mn ratio. As the synthesis parameters are largely the same for both the colloidal syntheses, a result of the increase in precursor solution volume results not only in an decrease in the Co:Mn ratio, but also in a decreased amount of surfactants avail-

Table 6.1: The effect of various synthesis parameters on resulting colloidal particles.

Increase in ...	Effect on colloidal particles
Scale	Loss in homogeneity
Heating rate	More well defined particle shape and more narrow size distribution
Amount of structure directing agent (oleylamine)	More well defined particle shape
Co:Mn ratio	Change in particle shape
Injection temperature	Smaller particles

Table 6.2: Comparison in selectivity(%) of catalyst found in literature and synthesised catalysts.

Catalyst	C_1	C_2-C_4		C_{5+}
Co/CNT (IWI)[58]	42		28	30
Co/SiO$_2$ (IWI)[57]	35		40	25
Colloidal Co/SiO$_2$[57]	44		41	15
Co:Mn/SiO$_2$ (IWI)[57]	20		35	45
Colloidal Co:Mn/SiO$_2$[57]	17		38	45
		olefins	paraffins	
Colloidal Fe/CNT[15]	31	60	2	7
Tetrahedral	18	35	2	45
Tetrahedral calcined	14	24	2	60
Hexagonal	35	55	4	6
Reference	25	30	5	40

able per metal precursor species. This is true for both the stabilising and structure directing surfactants. It is therefore interesting that the synthesis with a relatively lesser amount of surfactants, on average yielded same size to smaller particles. It is therefore possible that the decrease in relative surfactant amounts resulted in a change in colloidal shape as the hexagonal colloids possibly require fewer surfactants to stabilise its particles.

An explanation for the decrease in activity of the hexagonal particles compared to the tetrahedral particles could be the covering of the active cobalt sites with the abundantly present MnO in the hexagonal particles. This phenomenon was spotted with XPS. It showed that calcination possibly resulted in the migration of MnO to the surface of the hexagonal particles. Possibly this migration also occurred during reduction/catalytic testing.

6.2   Comparison of model catalyst with reference catalyst and literature

Compared to the reference catalyst, the fresh model catalysts showed an alternate crystal structure. XRD and XPS showed that the model catalysts undergo a structural change upon calcination. The effect of calcination was an increase in activity, therefore it seems that a mixed spinel structure is a more active FT phase. Yet, compared to the reference catalyst, the activity remained lower for the model systems.

Possibly, differences in activity are caused by varying degrees of available Co surface. Therefore it would be interesting to analyse the catalyst surfaces using chemisorption, however due to their small size, practical limitations prevent the use of chemisorption equipment. By supporting these particles, e.g. on CNTs, chemisortpion on these systems would be possible (see ourlook).

Table 6.2 shows the overall comparison between catalysts, either synthesised or found in literature, in terms of selectivity. All these results were achieved using low pressure tests, i.e. 1 bar, with varying temperatures as was described in the theory/experimental procedure section.

The tetrahedral and reference catalyst show a reasonably high lower olefin selectivity. This effect could

be ascribed to the promoting effect of MnO, yet other factors could be of influence:

Literature has shown that MnO promotion can have various effects on cobalt FT catalysts[21]. MnO shows electronic interaction by withdrawing electron density from Co, resulting in a lower hydrogenation rate, i.e. yielding a higher O/P ratio[61]. Additionally, promotion with MnO suppresses methane production and increases the C_{5+} fraction by shifting the alpha value. Consensus is that a low loading of MnO (Mn/Co up to 0.05) is sufficient to achieve the desirable shift in selectivity, i.e. increase of alpha (at equivalent reaction conditions) and some groups claim that a larger loading of MnO has no additional positive effect on the C_{5+} fraction selectivity[64, 60, 57]. For example, the Co/Mn particles synthesised by Werner et al. [57], both through colloidal and IWI synthesis, show significantly lower selectivity towards methane and higher towards C_{5+} production.

Furthermore, it has been shown in literature that a low loading of MnO enhances the activity of the active phase, but with an increasing loading the activity declines due to the covering of the cobalt surface with Mn species[60, 61, 64]. However, both low and high pressure catalytic performance of the bulk CoMnO catalysts showed an increase in activity with an increase in MnO loading. However, as co-precipitation yields a bulk catalyst, the abundantly present manganese oxide species can function as a support for cobalt. A decrease in MnO content can therefore lead to a decreased cobalt dispersion, which is in turn expected to lead to a decreased activity.

The chain growth probability of cobalt is highly susceptible to change by varying reaction conditions. For example, the alpha value for cobalt is dependent on temperature, where an increase in temperature results in a decrease in alpha. Consequently, high alpha FT reactions are performed at a lower temperature, e.g. 220 °C, than when a product stream of a lower average chain length is desired (e.g. C_2-C_4, 240 °C). It was observed that (almost all) CoMnO catalysts showed FTS behaviour rather than FTO behaviour, i.e. their main product fraction was C_{5+}. These reactions have all been performed at 240 °C, therefore it is expected that a decrease in reaction temperature will yield a larger C_{5+} (and a smaller C_2-C_4) fraction. High pressure measurements performed at both 220 °C and 240 °C confirmed these statements. Thus, an increased MnO loading in fact seems to have a enhancing effect on the alpha of a cobalt catalyst. However, data shown in Tables 4.2 and 4.4 does not directly confirm this statement.

The synthesised CoMnO catalysts thus seem to be FTS catalysts rather than FTO catalysts, where the alpha of the system is simple altered by increasing the reaction temperature. The catalysts with a high MnO loading outperform the cobalt catalysts found in literature in terms of C_{5+} selectivity.

However, potentially these observed results are due to differences in catalyst preparation. The systems described in literature all encompass supported catalysts, whereas unsupported CoMnO is used in this research. As a consequence, no spillover of MnO onto a surface or SMSI between the active phase and the support will occur. The synthesised CoMnO system are mixed phases with high interaction between Co and MnO, where support interactions may decrease this interaction. It may be that the absence of a support for these systems are of large influence on the observed selectivities.

7

Conclusion and outlook

In this work, the research on the synthesis of a model catalyst was described, in combination with a literature study on CoMnO systems for FT reactions, as well as a description of work performed on the synthesis, characterisation and testing of a reference bulk CoMnO system. Several conclusions could be drawn from the performed research.

Bulk CoMnO with varying Co:MnO ratios was synthesised as a reference system for colloidal particles. These systems possessed a mixed spinel CoMnO structure, as was confirmed with XRD. Using these bulk catalysts, reaction optima at elevated pressures were uncovered to be 240 °C and 10 bar for the production of lower olefins. Additionally, these systems have shown that the highest MnO loading (80 wt%) resulted in the best performing FTO catalyst in terms of activity and selectivity.

This research showed that using a polyol synthesis, colloidal CoMnO nanoparticles can reproducibly be made. By varying synthesis parameters, the size, shape, composition etc. of the resulting particles can be influenced. One of the parameters thoroughly researched in this work was the Co:Mn ratio of the colloids, effectively influencing the particle shape (TEM) and catalytic performance.

STEM-EDX showed that the colloids possess a uniform distribution of Co and Mn species. The crystal structure varied from the bulk CoMnO, as XRD showed that the colloids were composed of separate CoO and MnO phases. XPS verified the uniformity of the bulk and surface structure. It was found that calcination could be used to alter the crystal structure to a mixed spinel CoMnO structure. However, XPS indicated that for particles with very high MnO loadings (hexagonal particles, 76 at%), calcining could induce Mn migration to the Co surface.

Catalytic tests showed that the colloidal particles were less active than the reference bulk CoMnO compound, in particular the hexagonal particles. Efforts were made to increase the CO conversion of the hexagonal catalyst, such as decreasing the syngas flow and catalyst loading, to reliably acquire the selectivity. The hexagonal catalyst showed the highest lower olefin selectivity (55%) of the synthesised catalyst, together with the highest methane selectivity (35%) and lowest activity.

By calcining the tetrahedral particles, they became more active and the alpha value was (largely) increased. It was concluded that a mixed CoMnO spinel phase is more FT catalytically active. Additionally, TEM showed the large thermal stability of the colloidal catalysts. After heat treatments, such as calcination or

catalytic testing, the particles kept their structural integrity. However, TEM also showed that with increased temperature, the release of surfactants resulted in the aggregation of particles due to decreased electrostatic repulsion between colloids.

It was found in this research that by utilising a (high loading of) MnO, the alpha value of a catalyst can be increased. The catalysts, excluding the hexagonal colloidal particles, showed FTS behaviour. Therefore, as these catalysts were tested at 240 °C, these catalyst could prove to be excellent FTS catalysts at a lower temperature, e.g. 220 °C, as a decrease in temperature increases the alpha value further.

Outlook   A few suggestions for further research on this subject are outlined. These can be divided between suggestions for synthesis, characterisation and catalytic testing. For the synthesis, it would be tremendously interesting to further investigate synthesis parameters and their effect on the resulting colloidal particles in e.g. systematically increasing the Co:MnO ratio and studying the effect on particle shape, size, structure etc.

Also, another attempt at the deposition of the colloidal particles on a support, such as CNT, would be advised as it allows the colloidal particles to be tested with chemisorption, as the unsupported colloids were not compatible with the setup. This would allow the available Co surface to be quantified and could be used to explain differences in activity (see Discussion).

For this deposition, it might be an option to increase the loading on the CNTs (which has shown to be very low for the attempted depositions (verified with TGA-MS, see Appendix)), by repeating the deposition procedure with multiple batches of colloidal particles. In order to check the potential of this method, one could first deposit either the tetrahedral or hexagonal particles, followed by the deposition of the other particle type and use TEM to analyse the resulting systems. By comparing TEM images after the first and second deposition, it is possible to verify the method, as the TEM images after the second deposition should show the presence of an alternate Co species, while maintaining a comparable amount of the initial species.

In terms of characterisation, in-situ XRD would be interesting to analyse at what temperature the structure change of CoO and MnO to CoMnO occurs and how this process develops. Also, XRD/XPS on the spent particles would be very interesting to determine whether elemental migration occurred during catalytic testing. Potentially, chemisorption can also be used to this end. Additionally, STEM-EDX on the calcined particles could be used to show whether or not there is a significant redistribution of the Co and Mn species in the particles, e.g. the formation of Co/Mn rich areas.

In terms of catalytic testing, it would be interesting to also test the calcined hexagonal particles for FTO activity and selectivity, and both types of colloidal catalysts at elevated pressures. For this purpose, the particles would have to be supported. Another argument for the supporting of the colloidal particles may be that supporting should increase stability against sintering/agglomeration. By using the supported particles in low pressure tests, the effect of decreased sintering/agglomeration on the catalytic performance can be probed.

A tactic to tackle the observed low activity issue might be to reduce the catalysts at a lower temperature than what is currently used (350 °C). Since the research has shown that MnO can have a positive effect on the reducibility of Co (in bulk CoMnO), a lower temperature than 350 °C may be sufficient to fully convert CoO to the catalytically active Co, thereby decreasing the degree of agglomeration/sintering during reduction.

In parallel, TGA-MS could be used to determine the decomposition/release temperature of the surfactants present on the colloidal surface.

To research the effect of (an absence of) SMSI interaction, the colloidal particles could be deposited not only on CNT, but also on oxidic supports such as SiO_2, TiO_2 etc. Additionally, to check the FTS potential of the CoMnO catalyst with high MnO loadings, catalytic testing at decreased temperatures, e.g. 220 °C could be performed. Also, MnO loading variations and their effect on the selectivity could be researched.

8

List of Abbreviations and Symbols

°C	Degrees Celsius
Å	Angstrom
α	Chain growth probability
2θ	Angle
ASF-plot	Anderson-Schultz-Flory plot
BDO	1,4-butadienediol
CNF	Carbon nanofiber
CNT	Carbon nano tube
CTY	Cobalt time yield
DFT	Density functional theory
DMTO	Dimethyl ether to olefins
eV	Electronvolt
FID	Flame ionisation detector
FT	Fischer-Tropsch
FTO	Fischer-Tropsch to lower olefins
FTS	Fischer-Tropsch synthesis
FTY	Iron time yield
GHSV	Gas hourly space velocity
HDP	Homogeneous deposition precipitation
HSAG	High surface area graphite
i	Number of carbon atoms
ICP-MS	Inductively coupled plasma mass spectrometry
IWI	Incipient wetness impregnation
mg	Milligram
M_i	Volume percentage of i in product stream
μL	Microliter
min	Minutes

mL	Milliliter
mmol	Millimol
MTO	Methanol to olefins
N_i	Number of carbon atoms of fraction i
nm	Nanometer
O/P	Olefin to paraffin ratio
p	Pressure
Q	Volumetric flow
rpm	Revolutions per minute
SEM	Scanning electron microscopy
SEM-EDX	Scanning electron microscopy energy dispersive x-ray spectroscopy
SSITKA	Steady state isotopic transient kinetic analysis
STEM-EDX	Scanning transmission electron microscopy energy dispersive x-ray spectroscopy
T	Temperature
TCD	Thermal conductivity detector
TEM	Transmission electron microscopy
TGA-MS	Thermogravimetric analyser mass spectrometry
TOS	Time on stream
TPR	Temperature programmed reduction
w_i	Weight fraction of chain length i
XPS	X-ray photoelectron spectroscopy
XRD	X-ray diffraction

Bibliography

[1] H.M. Torres Galvis and K.P. De Jong. Catalysts for production of lower olefins from synthesis gas: A review. *ACS Catalysis*, 3(9):2130–2149, 2013.

[2] OPEC. World oil outlook, 2015.

[3] I. Chorkendorff and J.W. Niemantsverdriet. *Concepts of Modern Catalysis and Kinetics*. Wiley-VCH, second edition, 2007.

[4] M.E. Dry. Practical and theoretical aspects of the catalytic Fischer-Tropsch process. *Applied Catalysis A: General*, 138(2):319 – 344, 1996.

[5] U. Olsbye, S. Svelle, M. Bjorgen, P. Beato, T.V.W. Janssens, F. Joensen, S. Bordiga, and K.P. Lillerud. Conversion of methanol to hydrocarbons: How zeolite cavity and pore size controls product selectivity. *Angewandte Chemie - International Edition*, 51(24):5810–5831, 2012.

[6] P. Tian, Y. Wei, and Z. Liu. Methanol to Olefins(MTO): From fundamentals to commercialization. *ACS Catalysis*, 5(3), 2015.

[7] Y. Hirota, K. Murata, M. Miyamoto, Y. Egashira, and N. Nishiyama. Light olefins synthesis from methanol and dimethylether over SAPO-34 nanocrystals. *Catalysis Letters*, 140(1-2):22–26, 2010.

[8] H. Schulz. Short history and present trends of Fischer-Tropsch synthesis. *Applied Catalysis A: General*, 186(12):3 – 12, 1999.

[9] M.E. Dry. The Fischer-Tropsch process: 1950-2000. *Catalysis Today*, 71(34):227 – 241, 2002.

[10] A.K. Dalai and B.H. Davis. Fischer-Tropsch synthesis: A review of water effects on the performances of unsupported and supported Co catalysts. *Applied Catalysis A: General*, 348(1):1 – 15, 2008.

[11] N.E. Tsakoumis, M. Ronning, O. Borg, E. Rytter, and A. Holmen. Deactivation of cobalt based Fischer-Tropsch catalysts: A review. *Catalysis Today*, 154(34):162 – 182, 2010.

[12] S. Krishnamoorthy, M. Tu, M.P. Ojeda, D. Pinna, and E. Iglesia. An investigation of the effects of water on rate and selectivity for theFischer-Tropsch synthesis on cobalt-based catalysts. *Journal of Catalysis*, 211(2):422 – 433, 2002.

[13] A.Y. Khodakov, W. Chu, and P. Fongarland. Advances in the development of novel cobalt Fischer-Tropsch catalysts for synthesis of long-chain hydrocarbons and clean fuels. *Chemical Reviews*, 107(5):1692–1744, 2007.

[14] R.B. Anderson, R.A. Friedel, and H.H. Storch. Fischer-Tropsch reaction mechanism involving stepwise growth of carbon chain. *The Journal of Chemical Physics*, 19(3):313–319, 1951. cited By 73.

[15] M. Casavola, J. Hermannsdorfer, N. De Jonge, A.I. Dugulan, and K.P. De Jong. Fabrication of Fischer-Tropsch catalysts by deposition of iron nanocrystals on carbon nanotubes. *Advanced Functional Materials*, 25(33):5309–5319, 2015.

[16] B.H. Davis. Fischer-tropsch synthesis: Reaction mechanisms for iron catalysts. *Catalysis today*, 141(1-2):25–33, 2009.

[17] D.B. Bukur, L. Nowicki, R.K. Manne, and X.S. Lang. Activation studies with a precipitated iron catalyst for Fischer-Tropsch synthesis. II. reaction studies. *Journal of Catalysis*, 155(2):366–375, 1995.

[18] B. Todic, W. Ma, G. Jacobs, B.H. Davis, and D.B. Bukur. Effect of process conditions on the product distribution of Fischer-Tropsch synthesis over a Re-promoted cobalt-alumina catalyst using a stirred tank slurry reactor. *Journal of Catalysis*, 311:325–338, 2014.

[19] M. Feyzi, M.M. Khodaei, and J. Shahmoradi. Effect of preparation and operation conditions on the catalytic performance of cobalt-based catalysts for light olefins production. *Fuel Processing Technology*, 93(1):90–98, 2012.

[20] W. Ma, G. Jacobs, R.A. Keogh, D.B. Bukur, and B.H. Davis. Fischer-Tropsch synthesis: Effect of Pd, Pt, Re, and Ru noble metal promoters on the activity and selectivity of a 25%Co/Al$_2$O$_3$ catalyst. *Applied Catalysis A: General*, 437438:1 – 9, 2012.

[21] F. Morales Cano. *Manganese Promotion in Titania-Supported Cobalt Fischer-Tropsch Catalysis*. PhD thesis, Utrecht University, 2006.

[22] W.G. Zhou, J.Y. Liu, X. Wu, J.F. Chen, and Y. Zhang. An effective Co/MnOx catalyst for forming light olefins via Fischer-Tropsch synthesis. *Catalysis Communications*, 60:76–81, 2015.

[23] M. Feyzi, M. Irandoust, and A.A. Mirzaei. Effects of promoters and calcination conditions on the catalytic performance of iron-manganese catalysts forFischer-Tropsch synthesis. *Fuel Processing Technology*, 92(5):1136–1143, 2011.

[24] S. Shetty and R.A. van Santen. {CO} dissociation on Ru and Co surfaces: The initial step in the Fischer-Tropsch synthesis. *Catalysis Today*, 171(1):168 – 173, 2011.

[25] M. Ojeda, R. Nabar, A.U. Nilekar, A. Ishikawa, M. Mavrikakis, and E. Iglesia. {CO} activation pathways and the mechanism of Fischer-Tropsch synthesis. *Journal of Catalysis*, 272(2):287 – 297, 2010.

[26] J. Yang, Y. Qi, J. Zhu, Y. Zhu, D. Chen, and A. Holmen. Reaction mechanism of {CO} activation and methane formation on Co Fischer-Tropsch catalyst: A combined DFT, transient, and steady-state kinetic modeling. *Journal of Catalysis*, 308:37 – 49, 2013.

[27] S. Mousavi, A. Zamaniyan, M. Irani, and M. Rashidzadeh. Generalized kinetic model for iron and cobalt based Fischer-Tropsch synthesis catalysts: Review and model evaluation. *Applied Catalysis A: General*, 506:57 – 66, 2015.

[28] A.Y. Khodakov, B. Peregryn, A.S. Lermontov, J.-S. Girardon, and S. Pietrzyk. Transient studies of the elementary steps of Fischer-Tropsch synthesis. *Catalysis Today*, 106(14):132 – 136, 2005.

[29] B.H. Davis. Fischer-Tropsch synthesis: current mechanism and futuristic needs. *Fuel Processing Technology*, 71(13):157 – 166, 2001.

[30] J. Gaube and H.-F. Klein. Studies on the reaction mechanism of the Fischer-Tropsch synthesis on iron and cobalt. *Journal of Molecular Catalysis A: Chemical*, 283(12):60 – 68, 2008.

[31] J. Gaube and H.-F. Klein. Further support for the two-mechanisms hypothesis of Fischer-Tropsch synthesis. *Applied Catalysis A: General*, 374(12):120 – 125, 2010.

[32] B. Todic, W. Ma, G. Jacobs, B.H. Davis, and D.B. Bukur. Co-insertion mechanism based kinetic model of the Fischer-Tropsch synthesis reaction over Re-promoted Co catalyst. *Catalysis Today*, 228:32 – 39, 2014.

[33] J. Cheng, X. Gong, P. Hu, C. Martin Lok, P. Ellis, and S. French. A quantitative determination of reaction mechanisms from density functional theory calculations: Fischer-Tropsch synthesis on flat and stepped cobalt surfaces. *Journal of Catalysis*, 254(2):285 – 295, 2008.

[34] M. Zhuo, A. Borgna, and M. Saeys. Effect of the {CO} coverage on theFischer-Tropsch synthesis mechanism on cobalt catalysts. *Journal of Catalysis*, 297:217 – 226, 2013.

[35] I.M. Ciobica, G.J. Kramer, Q. Ge, M. Neurock, and R.A. van Santen. Mechanisms for chain growth in Fischer-Tropsch synthesis over Ru(0001). *Journal of Catalysis*, 212(2):136 – 144, 2002.

[36] M. Kollar, A. De Stefanis, H.E. Solt, M.R. Mihalyi, J. Valyon, and A.A.G. Tomlinson. The mechanism of theFischer-Tropsch reaction over supported cobalt catalysts. *Journal of Molecular Catalysis A: Chemical*, 333(12):37 – 45, 2010.

[37] S. Logdberg, M. Lualdi, S. Jaras, J.C. Walmsley, E.A. Blekkan, E. Rytter, and A. Holmen. On the selectivity of cobalt-based Fischer-Tropsch catalysts: Evidence for a common precursor for methane and long-chain hydrocarbons. *Journal of Catalysis*, 274(1):84 – 98, 2010.

[38] M. Sadeqzadeh, H. Karaca, O.V. Safonova, P. Fongarland, S. Chambrey, P. Roussel, A. Griboval-Constant, M. Lacroix, D. Curulla-Ferr, F. Luck, and A.Y. Khodakov. Identification of the active species in the working alumina-supported cobalt catalyst under various conditions of Fischer-Tropsch synthesis. *Catalysis Today*, 164(1):62 – 67, 2011.

[39] A.Y. Khodakov. Fischer-Tropsch synthesis: Relations between structure of cobalt catalysts and their catalytic performance. *Catalysis Today*, 144(34):251 – 257, 2009.

[40] S. Storster, . Borg, E.A. Blekkan, and A. Holmen. Study of the effect of water on fischer-tropsch synthesis over supported cobalt catalysts. *Journal of Catalysis*, 231(2):405–419, 2005. cited By 148.

[41] A.M. Saib, D.J. Moodley, I.M. Ciobc, M.M. Hauman, B.H. Sigwebela, C.J. Weststrate, J.W. Niemantsverdriet, and J. van de Loosdrecht. Fundamental understanding of deactivation and regeneration of cobalt Fischer-Tropsch synthesis catalysts. *Catalysis Today*, 154(34):271 – 282, 2010.

[42] T. Fu, Y. Jiang, J. Lv, and Z. Li. Effect of carbon support on Fischer-Tropsch synthesis activity and product distribution over Co-based catalysts. *Fuel Processing Technology*, 110:141–149, 2013.

[43] J.A. Diaz, M. Martinez-Fernandez, A. Romero, and J.L. Valverde. Synthesis of carbon nanofibers supported cobalt catalysts forFischer-Tropsch process. *Fuel*, 111:422 – 429, 2013.

[44] E. Iglesia, S.L. Soled, and R.A. Fiato. Fischer-Tropsch synthesis on cobalt and ruthenium. metal dispersion and support effects on reaction rate and selectivity. *Journal of Catalysis*, 137(1):212 – 224, 1992.

[45] Z. Yan, Z. Wang, D.B. Bukur, and D.W. Goodman. Fischer-Tropsch synthesis on a model Co/SiO_2 catalyst. *Journal of Catalysis*, 268(2):196 – 200, 2009.

[46] A.M. Venezia, V. La Parola, L.F. Liotta, G. Pantaleo, M. Lualdi, M. Boutonnet, and S. Jaras. Co/SiO_2 catalysts forFischer-Tropsch synthesis; effect of Co loading and support modification by TiO_2. *Catalysis Today*, 197(1):18 – 23, 2012.

[47] T. Fu and Z. Li. Review of recent development in Co-based catalysts supported on carbon materials for Fischer-Tropsch synthesis. *Chemical Engineering Science*, 135:3 – 20, 2015.

[48] E. Iglesia. Design, synthesis, and use of cobalt-basedFischer-Tropsch synthesis catalysts. *Applied Catalysis A: General*, 161(12):59 – 78, 1997.

[49] P. Munnik, P.E. De Jongh, and K.P. De Jong. Control and impact of the nanoscale distribution of supported cobalt particles used in Fischer-Tropsch catalysis. *Journal of the American Chemical Society*, 136(20):7333–7340, 2014.

[50] P. Lu, J. Sun, P. Zhu, T. Abe, R. Yang, A. Taguchi, T. Vitidsant, and N. Tsubaki. Sputtered nano-cobalt on H-USY zeolite for selectively converting syngas to gasoline. *Journal of Energy Chemistry*, 2015. Article in Press.

[51] H. Janani, A.R. Rezvani, G.H. Grivani, and A.A. Mirzaei. Fischer-Tropsch synthesis of hydrocarbons over new Co/Ce bimetallic catalysts derived from dipicolinate and carbonyl metal complexes. *Journal of Inorganic and Organometallic Polymers and Materials*, 25(5):1169–1182, 2015.

[52] P. Munnik, N.A. Krans, P.E. De Jongh, and K.P. De Jong. Effects of drying conditions on the synthesis of Co/SiO_2 and Co/Al_2O_3 Fischer-Tropsch catalysts. *ACS Catalysis*, 4(9):3219–3226, 2014. cited By 8.

[53] J.P. Den Breejen, P.B. Radstake, G.L. Bezemer, J.H. Bitter, V. Froseth, A. Holmen, and K.P. De Jong. On the origin of the cobalt particle size effects in Fischer-Tropsch catalysis. *Journal of the American Chemical Society*, 131(20):7197–7203, 2009.

[54] P. Munnik, P.E. De Jongh, and K.P. De Jong. Recent developments in the synthesis of supported catalysts. *Chemical Reviews*, 115(14):6687–6718, 2015. cited By 0.

[55] G.L. Bezemer, J.H. Bitter, H.P.C.E. Kuipers, H. Oosterbeek, J.E. Holewijn, X. Xu, F. Kapteijn, A.J. Van Diilen, and K.P. De Jong. Cobalt particle size effects in the Fischer-Tropsch reaction studied with carbon nanofiber supported catalysts. *Journal of the American Chemical Society*, 128(12):3956–3964, 2006.

[56] A. Dinse, M. Aigner, M. Ulbrich, G.R. Johnson, and A.T. Bell. Effects of Mn promotion on the activity and selectivity of Co/SiO_2 for fischer-tropsch synthesis. *Journal of Catalysis*, 288:104–114, 2012.

[57] S. Werner, G.R. Johnson, and A.T. Bell. Synthesis and characterization of supported cobalt-manganese nanoparticles as model catalysts for Fischer-Tropsch synthesis. *ChemCatChem*, 2014.

[58] Tom van Deelen. Niobia-promoted Co/CNT catalysts for the Fischer-Tropsch synthesis. Master's thesis, Utrecht University.

[59] D.J. Moodley, J. van de Loosdrecht, A.M. Saib, M.J. Overett, A.K. Datye, and J.W. Niemantsverdriet. Carbon deposition as a deactivation mechanism of cobalt-based Fischer-Tropsch synthesis catalysts under realistic conditions. *Applied Catalysis A: General*, 354(12):102 – 110, 2009.

[60] G.L. Bezemer, P.B. Radstake, U. Falke, H. Oosterbeek, H.P.C.E. Kuipers, A.J. Van Dillen, and K.P. De Jong. Investigation of promoter effects of manganese oxide on carbon nanofiber-supported cobalt catalysts for Fischer-Tropsch synthesis. *Journal of Catalysis*, 237(1):152–161, 2006.

[61] F. Morales Cano, O.L.J. Gijzeman, F.M.F. De Groot, and B.M. Weckhuysen. Manganese promotion in cobalt-based Fischer-Tropsch catalysis. *Studies in Surface Science and Catalysis*, 147:271–276, 2004.

[62] F. Morales Cano, F.M.F. De Groot, O.L.J. Gijzeman, A. Mens, O. Stephan, and B.M. Weckhuysen. Mn promotion effects in Co/TiO$_2$ Fischer-Tropsch catalysts as investigated by XPS and STEM-EELS. *Journal of Catalysis*, 230(2):301–308, 2005.

[63] A. Rose, J. Thiessen, A. Jess, and D. Curulla-Ferr. Unpromoted and Mn-promoted cobalt catalyst supported on carbon nanotubes for Fischer-Tropsch synthesis. *Chemical Engineering and Technology*, 37(4):683–691, 2014.

[64] J. Thiessen, A. Rose, J. Meyer, A. Jess, and D. Curulla-Ferr. Effects of manganese and reduction promoters on carbon nanotube supported cobalt catalysts in Fischer-Tropsch synthesis. *Microporous and Mesoporous Materials*, 164:199–206, 2012.

[65] Y. Liu, T.i Hanaoka, T. Miyazawa, K. Murata, K. Okabe, and K. Sakanishi. Fischer-Tropsch synthesis in slurry-phase reactors over Mn- and Zr-modified Co/SiO$_2$ catalysts. *Fuel Processing Technology*, 90(78):901 – 908, 2009.

[66] E.R. Stobbe, B.A. De Boer, and J.W. Geus. The reduction and oxidation behaviour of manganese oxides. *Catalysis today*, 47(1-4):161–167, 1999.

[67] R.A. Dictor and A.T. Bell. Fischer-Tropsch synthesis over reduced and unreduced iron oxide catalysts. *Journal of Catalysis*, 97(1):121–136, 1986. cited By 263.

[68] D.V.N. Vo and A.A. Adesina. Fischer-Tropsch synthesis over alumina-supported molybdenum carbide catalyst. *Applied Catalysis A: General*, 399(1-2):221–232, 2011. cited By 20.

[69] J.J. Spivey and S.K. Agarwal. *Catalysis*, volume 27. The Royal Society of Chemistry, 2005.

[70] A. De Klerk. *Fischer-Tropsch Refining*. Wiley-VCH Verlag, 2012.

[71] M.J. Keyser, R.C. Everson, and R.L. Espinoza. Fischer-Tropsch kinetic studies with cobalt-manganese oxide catalysts. *Industrial and Engineering Chemistry Research*, 39(1):48–54, 2000. cited By 51.

[72] J. Cheng, P. Hu, P. Ellis, S. French, G. Kelly, and C.M. Lok. Density functional theory study of iron and cobalt carbides for Fischer-Tropsch synthesis. *Journal of Physical Chemistry C*, 114(2):1085–1093, 2010. cited By 50.

[73] C. De Mello Donega, P. Liljeroth, and D. Vanmaekelbergh. Physicochemical evaluation of the hot-injection method, a synthesis route for monodisperse nanocrystals. *Small*, 1(12):1152–1162, 2005.
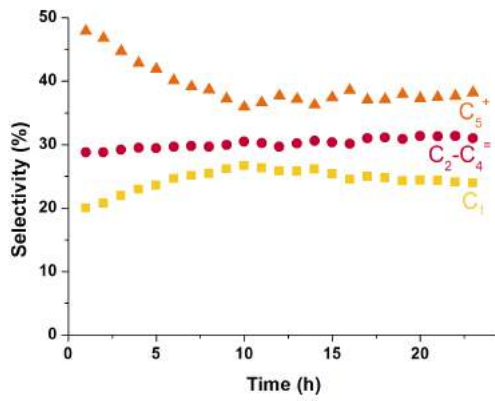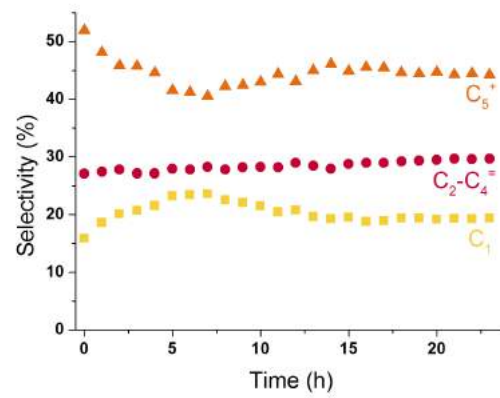
9

Appendices

9.1 ICP-MS

Table 9.1: ICP-MS elemental analysis.

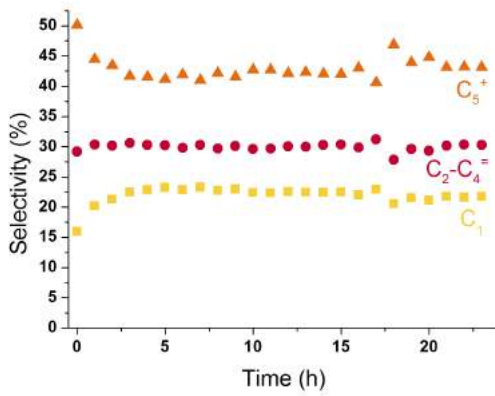| Catalyst	Co (wt%)	Mn (wt%)
Cat 20/80	25	75
Cat 35/65	41	59
Cat 50/50	56	44
Cat 65/35	71	29
	Co (at%)	Mn (at%)
Tetrahedral	38	62
Hexagonal	24	76

9.2   Low pressure testing co-precipitated catalysts

(a) Selectivity Cat 20/80

(b) Selectivity Cat 35/65

(c) Selectivity Cat 50/50
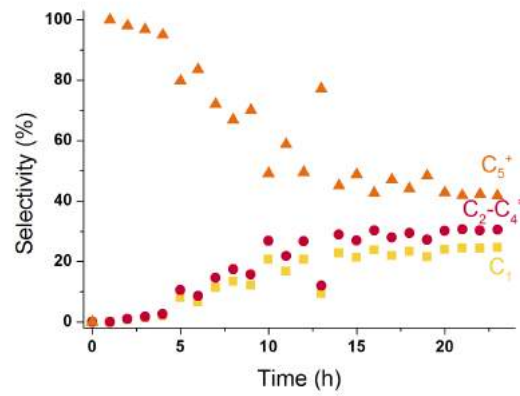
(d) Selectivity Cat 65/35

Figure 9.1: Selectivity co-precipitated catalysts at low pressure

9.3   High pressure testing (Flowrence) co-precipitated catalysts
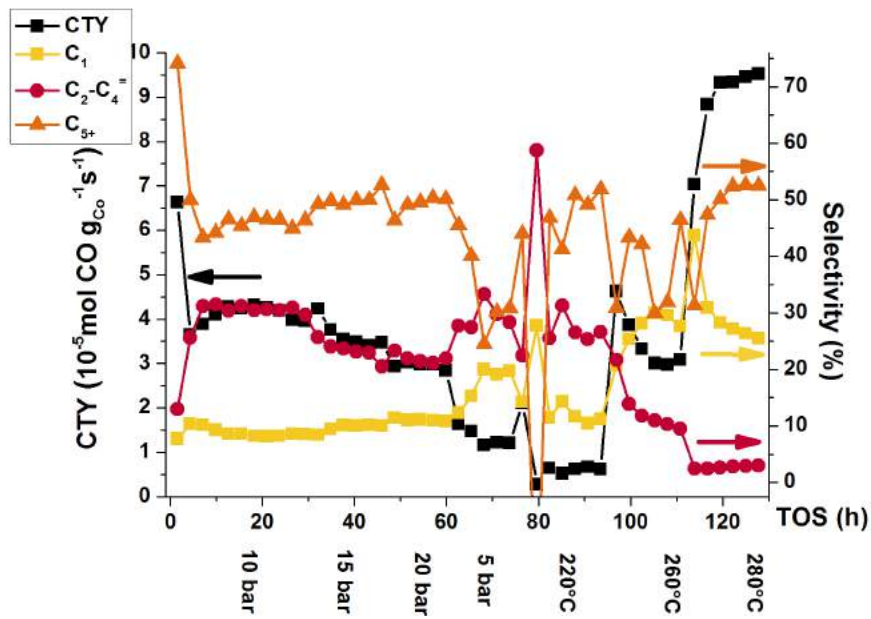
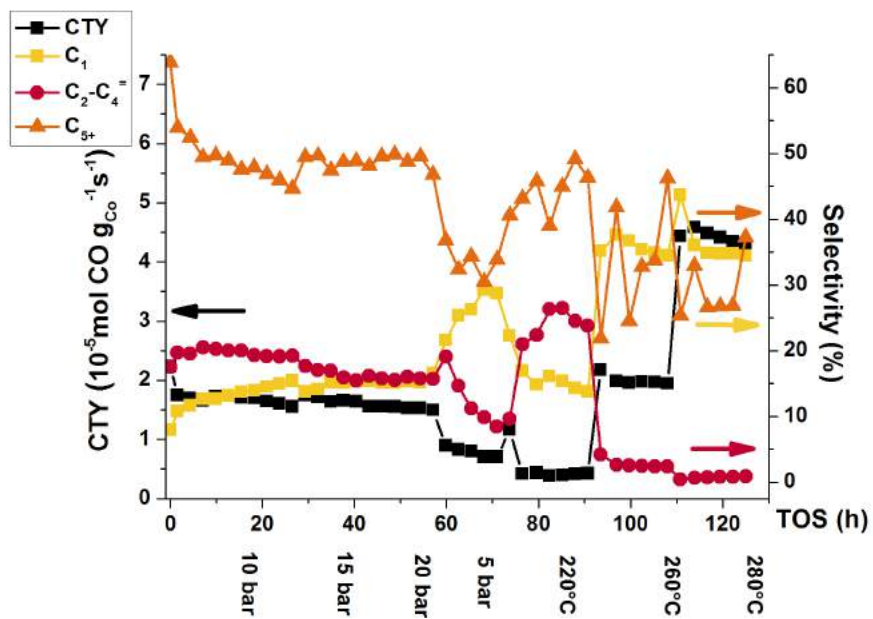Figure 9.2: Full high pressure catalytic measurement of Cat 20/80. Relevant condition variations are visible in the Figure. GHSV=2500h^{-1}, H$_2$:CO=2
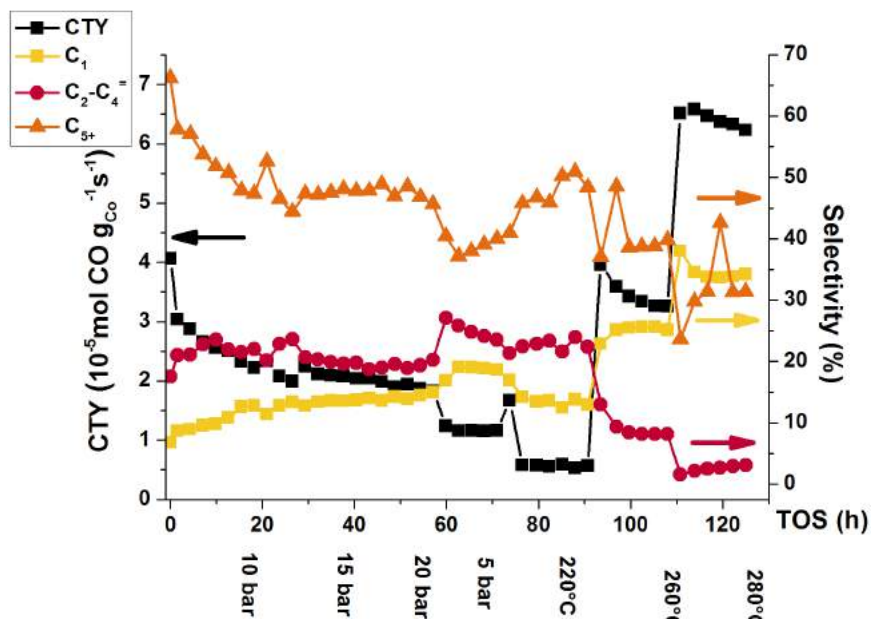
Figure 9.3: Full high pressure catalytic measurement of Cat 35/65. Relevant condition variations are visible in the Figure. GHSV=2500h^{-1}, H$_2$:CO=2
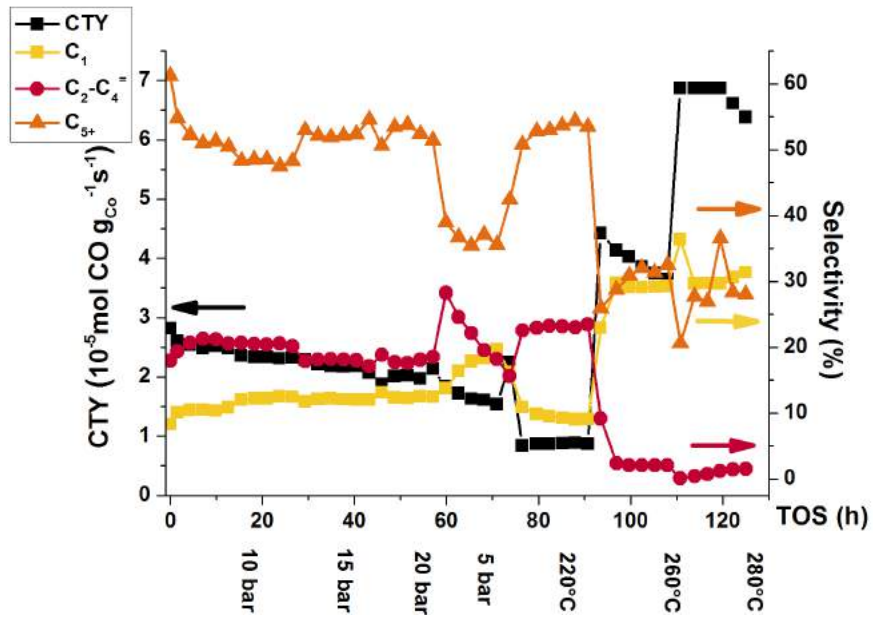
Figure 9.4: Full high pressure catalytic measurement of Cat 50/50. Relevant condition variations are visible in the Figure. GHSV=2500h^{-1}, H$_2$:CO=2

Figure 9.5: Full high pressure catalytic measurement of Cat 65/35. Relevant condition variations are visible in the Figure. GHSV=2500h^{-1}, H$_2$:CO=2

9.4   Particle size distribution

Something to note when reporting the particle sizes, is the presence of very small particles at the edges of assemblies of particles. This is seen for both tetrahedral and hexagonal particles: Figure 9.6.

(a)   (b)
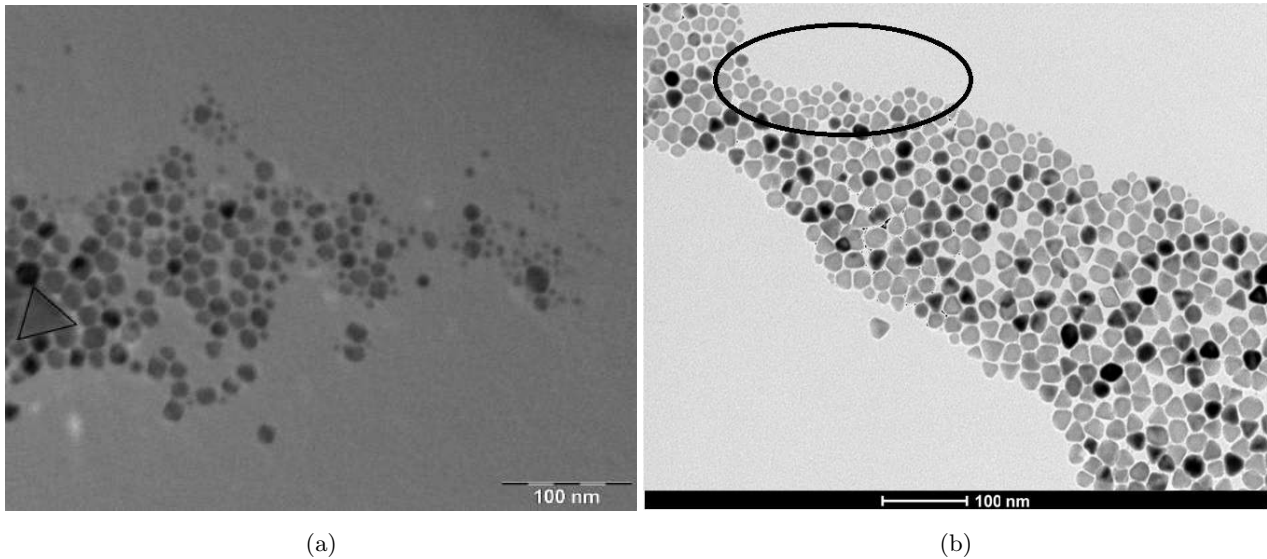
Figure 9.6: The presence of small particles, predominantly at the edges of particle assemblies.

Naturally, these small particles will have an effect on the average particle size, however, these small particles are only found in relatively small amounts, thus will not contribute largely to the particle size distribution.

9.5   TPR

Figure 9.7 shows the TPR measurement for the tetrahedral and hexagonal colloids, normalised per gram of catalyst.
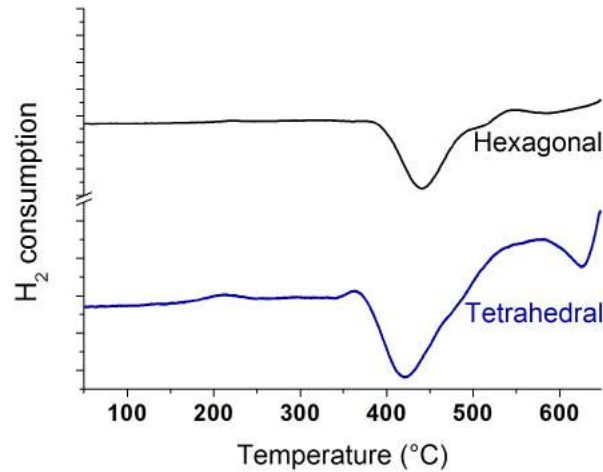
Figure 9.7: Temperature programmed reduction of tetrahedral and hexagonal colloidal particles.

For both samples, two remarkable features are present in the measurement: no noteworthy reduction peaks are present and a large amount of gas production occurs during the measurement. As a thermal conductivity detector (TCD) is used, it is not known what gas is released. It is suspected, however, that -as these colloidal particles had no pre-treatment- the released fraction stems from the release of the surfactants on the catalyst surface. As this release peak overlaps with the area where a reduction peak of CoO $\rightarrow$ Co is expected, no relevant information on the reducibility of the cobaltoxide can be uncovered, therefore, from these measurements, it is not known what the effect of manganese oxide is on the reducibility of cobalt.

9.6   TGA-MS

TGA measurements were performed using a Perkin Elmer Pyris 1TGA instrument. TGA-MS was used to determine the release/decomposition temperature of the surfactants present on the colloidal surface. Additionally, TGA-MS was used to determine the loading of colloidal CoMnO on CNTs. For the measurement analysing the release/decomposition temperature of the surfactants, the aim was to simulate the in-situ reduction step to verify whether the surfactants had released post-reduction and whether the cobaltoxide had reduced to metallic cobalt. As Figure 9.8 (left) shows, the measurement did not ramp up to the desired temperature, thus making the measurement incomplete. The measurement on the right gives a loading of 1.7wt% of colloids/CNT.
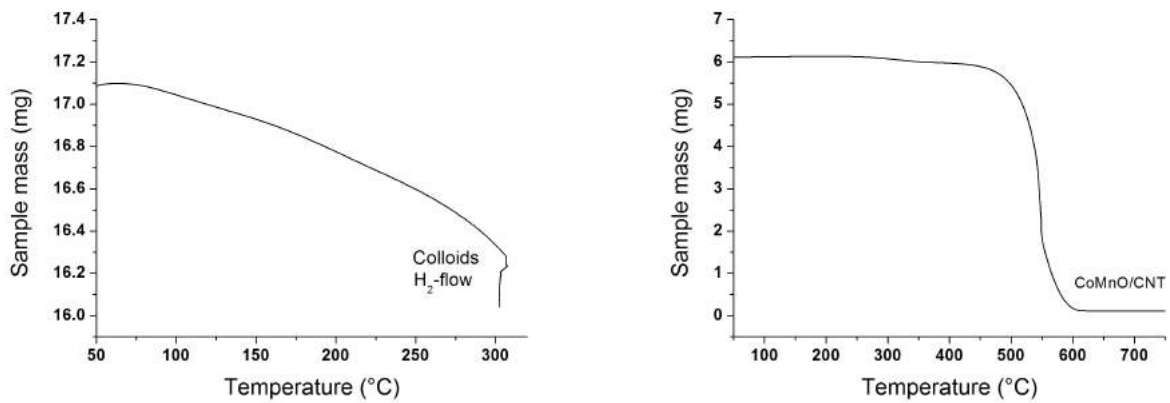
Figure 9.8: TGA-MS measurements for unsupported colloids (**left**) and colloids/CNT (**right**).

9.7   High pressure testing (Flowrence) tripods

Temperature dependence   Figure 9.9 gives the activity and selectivity of the unsupported tripod cata-lysts at various temperatures. For lower olefin selectivity comparison, the high pressure measurement of the reference catalyst is also added. Additionally tripod/CNT catalyst were tested, however these were either inactive, or had an activity too low to observe.
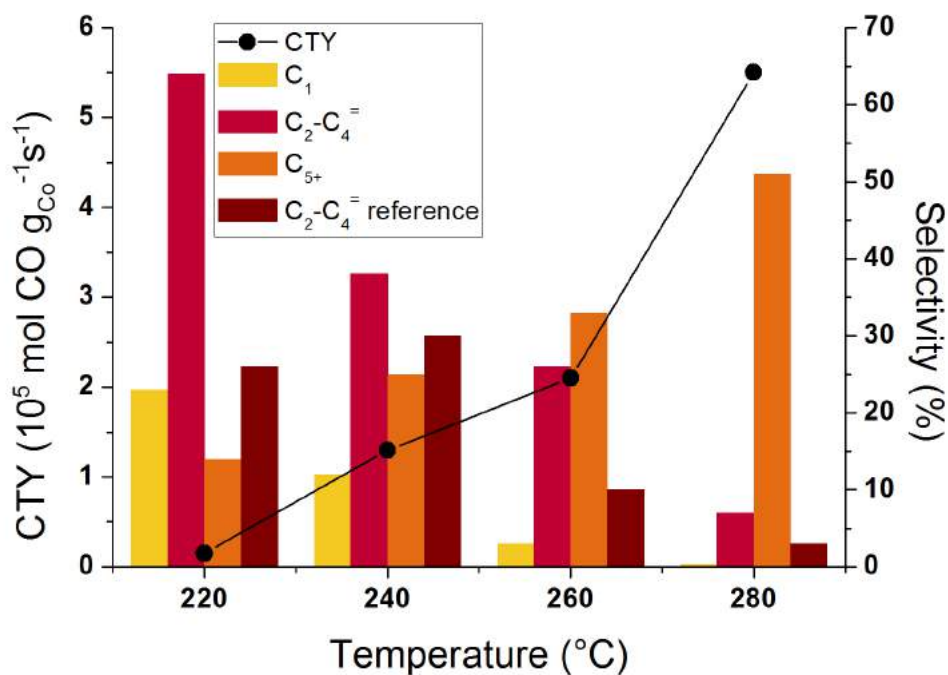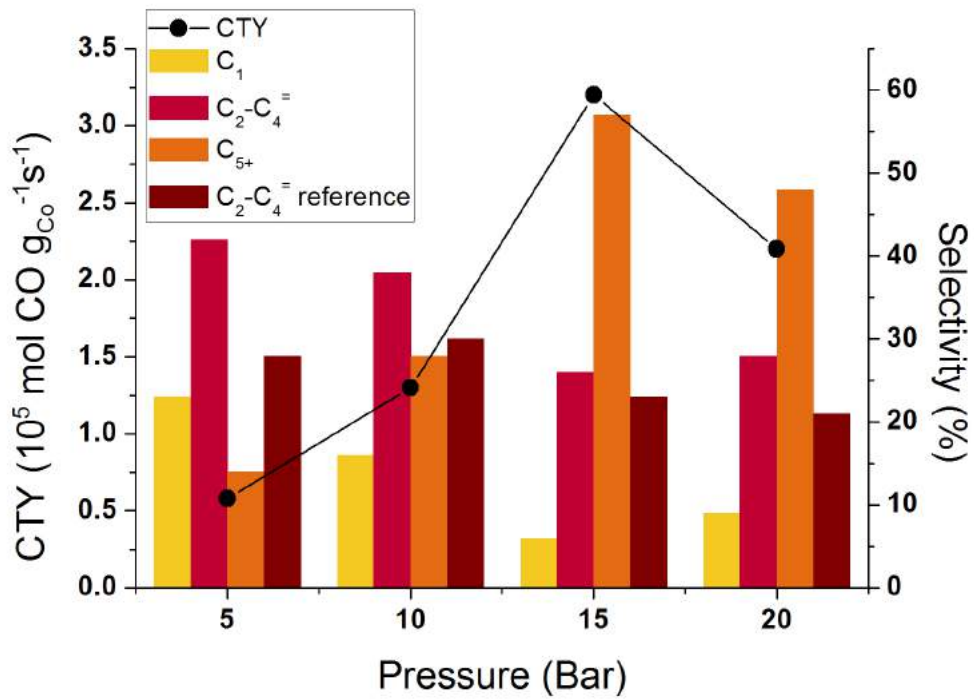

Figure 9.9: High pressure temperature dependent catalytic performance of tripod colloids together with lower olefin selectivity of reference catalyst. p=10 bar, GHSV=2500h^{-1}, TOS=15 h.

Pressure dependence   Figure 9.10 shows the activity and selectivity of the tripod catalyst with varying pressures.

Figure 9.10: High pressure pressure dependent catalytic performance of tripod colloids together with lower olefin selectivity of reference catalyst. T=240 °C, GHSV=2500h^{-1}, TOS=15 h.

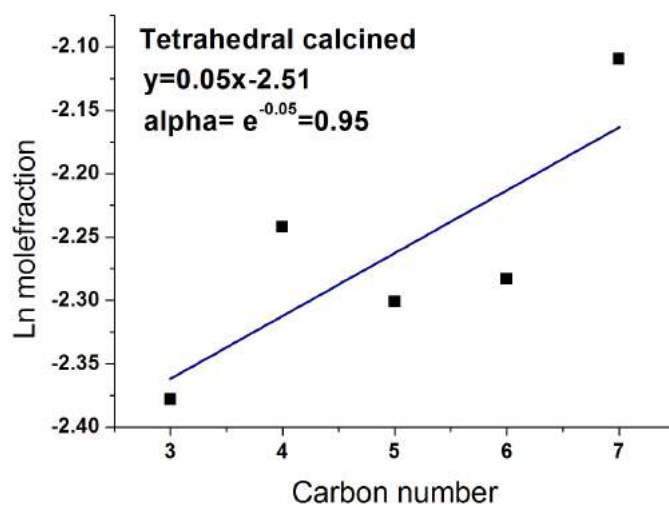## 9.8   Alpha calculation calcined tetrahedral catalyst

Figure 9.11

9.9   Spent catalyst

Figure 9.12 shows a TEM image of the spent tripod particles used for high pressure testing. Clearly, the structural integrity is no longer present: the particles have deformed and aggregated. It is not known whether the deformation of the colloidal particles occurred during reduction or during Fischer-Tropsch reactions. In order to assess which step in the catalytic testing was responsible, these results were compared with TEM images of spent catalysts retrieved from the low pressure setup.
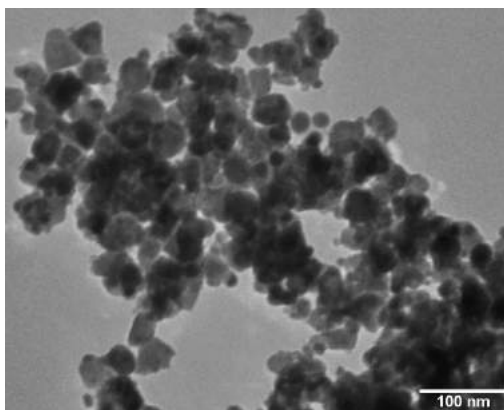

Figure 9.12: TEM image of spent tripod colloidal particles (Flowrence).